

Visible and near-infrared reflectance spectra of igneous rocks and their powders

Yan Zhuang^a, Hao Zhang^{a,b,*}, Pei Ma^a, Te Jiang^a, Yazhou Yang^c, Ralph E. Milliken^d, Weibiao Hsu^{b,e,f}

^a School of Earth Sciences, China University of Geosciences, Wuhan, China

^b CAS Center for Excellence in Comparative Planetology, Hefei, China

^c Key Laboratory of Space Weather, National Space Science Center, Chinese Academy of Sciences, Beijing, China

^d Department of Earth, Environmental, and Planetary Sciences, Brown University, Providence, RI, USA

^e Purple Mountain Observatory, Chinese Academy of Sciences, Nanjing, China

^f Deep Space Exploration Laboratory, University of Science and Technology, Hefei, China



ARTICLE INFO

Keywords:

Radiative transfer
Reflectance Spectroscopy
Planetary surfaces
Moon
Regolith

ABSTRACT

Most solid planetary bodies in the solar system are covered by a layer of fine particles and the topic of light scattering by small particles has been thoroughly studied in the past decades. In contrast, light reflection from intact rocks has received much less attention, though the spectral features of fresh rocks are more diagnostic than that of highly space-weathered regolith grains. As high spatial-resolution spectral images obtained by modern space-borne and *in-situ* sensors have become available, it is important to understand the spectral feature links between rocks and powders made by crushing the rocks. In this work, we selected 13 terrestrial igneous rocks with a 1 μm absorption feature and measured the visible and near-infrared reflectance spectra of their slabs and powders in three size fractions, 0–45 μm, 90–125 μm, and 450–900 μm. We have found that the spectral characteristics of these samples can be divided into two groups. For slabs with reflectance lower than 0.1 at 0.5 μm, they have less pronounced 1 μm absorption feature. For slabs with reflectance higher than 0.1, they have pronounced 1 μm feature, consistent with that of their powdered counterparts. By using the equivalent-slab and the Hapke model, we obtained the optical constants and single scattering albedo values of the samples. The dependence of single scattering albedo on effective absorption thickness indicates that the differences between the spectral characteristics of rock slabs and powdered samples are likely controlled by the degree of weak surface scattering contributions. We reconstructed the spectrum of a powdered lunar meteorite which best matches the Chang'E-4 rock and found that the reconstructed rock spectra are very close to the rock spectrum observed *in-situ* by Chang'E-4.

1. Introduction

The visible and near-infrared (VNIR) reflectance spectroscopy from 0.4 to 2.5 μm has been widely used in remote identification of planetary surface materials, as within the VNIR spectral range the Sun emits most of its electromagnetic energy and many planetary materials have diagnostic spectral features. For example, olivine has a diagnostic absorption band at 1 μm and pyroxene has diagnostic absorption bands at 1 μm and 2 μm (e.g., Adams, 1974; Pieters, 1983; Longhi et al., 2001; Paton et al., 2011; Burbine, 2017). In order to interpret remote sensing planetary analog spectra, numerous laboratory measurements on planetary analog

materials have been carried out and most of these measurements were made on particulate samples for a number of reasons: (1) most solid bodies in the solar system are covered by layers of regolith grains produced by prolonged impact and space weathering processes (e.g., McKay et al., 1991; Pieters et al., 1993; Keller and McKay, 1997; Hapke, 2001; Chapman, 2004; Pieters and Nobel, 2016), and as a result, the reflectance spectra are dominated by contributions from fine particle scattering (e.g., Noble et al., 2001); (2) mixtures of analogs with different mineralogical compositions can be easily achieved using powdered samples; (3) when illuminated by a light beam with finite size (typically ~1 cm or less in diameter) in a laboratory spectroscopic measurement, a

* Corresponding author at: School of Earth Sciences, China University of Geosciences, Wuhan, China.

E-mail address: zhanghao@cug.edu.cn (H. Zhang).

homogeneous particulate surface layer can be easily made; (4) in the past decades, significant progress has been made in theory of light scattering by small particles, and as a result, the interpretations of reflectance spectra of small particles have been found quite successful (Hapke, 2012);

In contrast, quantitative modeling of reflectance spectra of intact rocks in the VNIR have not been extensively carried out for several reasons. First, except for the very small monolith asteroids, most solid planetary bodies are covered by regolith grains produced by impacts and space weathering, as evidenced by recent close-up images of small bodies (e.g., Itokawa (~ 300 m), Bennu (~ 500 m), etc.). For most celestial bodies, the Earth-based telescopic observations before the space age were only able to measure the disk-integrated reflectance spectra and thus the measured reflectance was dominated by small particle scattering (e.g., Lester et al., 1979; Helfenstein et al., 1996; Spjuth et al., 2012). Second, although surfaces of natural rocks are also granular materials at a microscopic scale, their microstructures are very different from that of packed layers of individual discrete grains. Therefore, the application of the conventional radiative transfer approach based on the concept of single and multiple scatterings is not straightforward to intact rocks. Third, the spatial resolutions of most planetary detectors are not high enough to directly measure rocks.

As more space-borne and *in-situ* planetary spectra with high spatial resolutions have become available, the accurate interpretation of VNIR spectra for rocks has become increasingly important. On the one hand, although rocks may have patina and dust caused by space weathering, they are still generally fresher than regolith and have more diagnostic spectral features (e.g., Pieters et al., 1993; Wentworth et al., 1999; Hapke, 2001; Chapman, 2004). On the other hand, many lunar meteorites and returned lunar rocks are so rare and precious that oftentimes their laboratory spectra are only available for measurements made on either slabs or powders, but not both. Therefore, in order to compare laboratory and remote sensing spectra to quantitatively retrieve mineralogical compositions of a planetary surface, the relationship between the spectra of rocks and their powders needs to be well understood.

Recently, the Yutu-2 rover of the Chang'E-4 mission measured the reflectance spectra of a rock near the landing site in Von Kármán crater inside the South Pole-Aitken basin (Di et al., 2019). This rock has much deeper absorption features than the surrounding regolith and thus may better reveal the surface mineralogy. By searching the Reflectance Experiment Laboratory (RELAB) spectra of all available Moon-related materials, we found that the lunar meteorite Yamato-86032#117 was one of the samples whose spectra best matched that of the Chang'E-4 rock (Ma et al., 2020). Unfortunately, the meteorite spectrum was only available for measurement on powders and thus a direct comparison with the intact meteorite was unavailable. This has motivated us to investigate the spectral feature relationship between intact rock and their powders with different size distributions.

In this work, we selected 13 types of terrestrial igneous rocks with different surface albedos and $1\text{ }\mu\text{m}$ absorption strengths and measured the VNIR spectra of both the rocks in slab form and powders made by crushing and sieving the rocks. By analyzing the spectral features of these samples using the equivalent slab model and the Hapke model, we tried to understand the similarities and differences between the spectral features of the rock and the powdered material with different particle sizes. We also applied our findings to data analysis of the Chang'E-4 measurement.

2. Samples, instrument, and measurement descriptions

2.1. Samples and sample preparations

Most rocks on the lunar surface are igneous (e.g., Jolliff et al., 2006). The reflectance spectra of the Chang'E-4 rock mentioned earlier have a deep absorption around $1\text{ }\mu\text{m}$ (Ma et al., 2020). Therefore, we selected

13 igneous rocks with varying surface albedos and varying strengths of the $1\text{ }\mu\text{m}$ absorption. These samples mainly consist of pyroxene, olivine, and plagioclase. The selected rocks (Fig. 1) are: Dunite, Peridotite, Olivine pyroxenolite, Picrite porphyrite, Kimberlite, Gabbro, Diabase, Olivine basalt, Andesite basalt, Trachyte, Pyroxene syenite, Orthophyre, and Lamprophyre. Such a selection may help us understand the spectral feature connections between rock chunks and powdered samples with various brightness.

To perform reflectance spectroscopic measurements on chunk samples, we cut the rocks into slabs with a thickness of 1.5 cm (Fig. 2) to be both optically thick and easily placed on the sample plate in the instrument. Each slab has a surface area larger than 2 cm by 2 cm to ensure a 1.5 cm -diameter incident beam can be comfortably accommodated. The cutting process removed parts with visible signs of weathering to ensure a fresh surface to be measured. The surface being measured was slightly polished so that the surface roughness was reduced while no specular reflection was visible.

The leftover bits and pieces from the slab cutting were scrutinized and those with fresh appearance and no visible evidence of weathering alterations were picked out and broken into flakes using a geological hammer and then pulverized using an agate mortar. The powders were wet-sieved into three different size fractions (Fig. 3): $0\text{-}45\text{ }\mu\text{m}$ (Size 1), $90\text{-}125\text{ }\mu\text{m}$ (Size 2), and $450\text{-}900\text{ }\mu\text{m}$ (Size 3). We also label the slab sample as Size 4. These four size fractions may be representative of typical planetary regolith (Papike et al., 1982; Jolliff et al., 2006) and the spacings between them are large enough to minimize any potential overlaps of their individual spectral features.

The mineral and chemical compositions of the rocks are given in Table 1 and Table 2, respectively. The chemical compositions were measured by wet chemistry method.

2.2. Instrument and measurement

The bi-directional reflectance spectrometer system used in this work

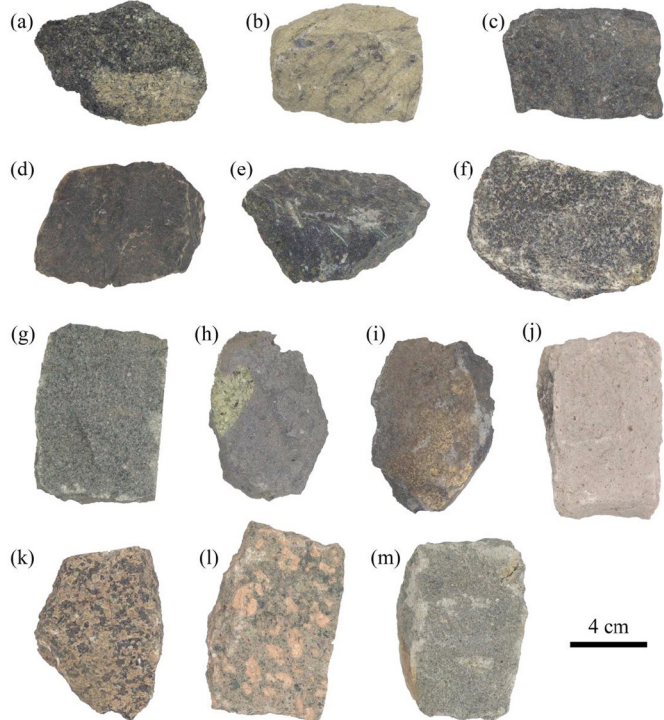


Fig. 1. Photos of 13 igneous rocks in their original state: (a) Dunite; (b) Peridotite; (c) Olivine pyroxenolite; (d) Picrite porphyrite; (e) Kimberlite; (f) Gabbro; (g) Diabase; (h) Olivine basalt; (i) Andesite basalt; (j) Trachyte; (k) Pyroxenite syenite; (l) Orthophyre; (m) Lamprophyre.

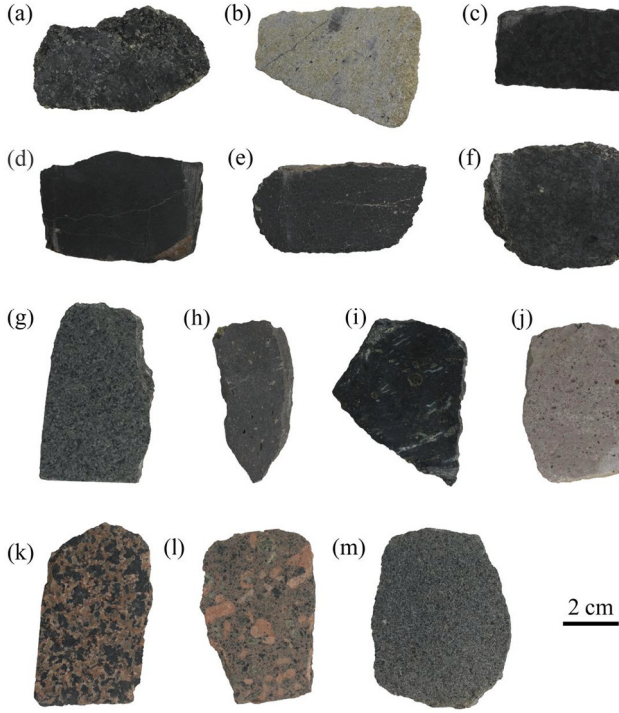


Fig. 2. Photos of 13 igneous rocks that have been cut into slabs with a thickness of 1.5 cm for reflectance measurement: (a) Dunite; (b) Peridotite; (c) Olivine pyroxenolite; (d) Picrite porphyrite; (e) Kimberlite; (f) Gabbro; (g) Diabase; (h) Olivine basalt; (i) Andesite basalt; (j) Trachyte; (k) Pyroxenite syenite; (l) Orthophyre; (m) Lamprophyre.

(Fig. 4) was an earlier version of the instrument that has been described in greater details (Jiang et al., 2022). It mainly consists of a light source, a goniometer, and a spectrometer to perform reflectance measurement in the principal plane. The light source is a highly stable Newport 66502-250Q-R1 quartz tungsten halogen lamp with an adjustable power range from 0–250 W and in this work the power was fixed at 50 W. Light from the bulb is inserted into a fiber optic cable with a collimator and directed to the sample surface with a typical spot diameter of ~1.5 cm. The sample holder used in this work has a depth of 3 mm. The goniometer is made up of two rotary stages with bars that carry the incident and viewing optical components. Both the incident and viewing zenith angles can be manually adjusted from 0° to 70° continuously. The reflected light is collected by a bare fiber and transmitted to a Spectral Evolution SR-2500 spectrometer. The spectral resolutions are 3.5 nm from 350 to 1000 nm and 22 nm at 1500 and 2100 nm. Bi-directional reflectance distribution function measurements on Labsphere Spectralon plaque with a 99% nominal reflectance agreed well with published data (Brueggel et al., 2001; Zhang and Voss, 2005; Jiang et al., 2019).

All reflectance measurements were made at an incident zenith angle of 0° and a viewing zenith of 30° in the principal plane. We first measured the intensities from the sample (I_{Sample}) and from the Labsphere Spectralon plaque ($I_{\text{Spectralon}}$) and used their ratio as the relative reflectance (Zhang et al., 2014). The reflectance factor (REFF) of the sample, which is the ratio of the reflectance of the sample surface to that of a perfect Lambertian surface under the same illumination and viewing conditions (Hapke, 2012), can be obtained as

$$\text{REFF}_{\text{Sample}}(i = 0^\circ, e = 30^\circ, \lambda) = \frac{I_{\text{Sample}}(i = 0^\circ, e = 30^\circ, \lambda)}{I_{\text{Spectralon}}(i = 0^\circ, e = 30^\circ, \lambda)} \text{REFF}_{\text{Spectralon}}^{RELAB}(i = 30^\circ, e = 0^\circ, \lambda), \quad (1)$$

where i and e are the incident and viewing zenith angles, and $\text{REFF}_{\text{Spectralon}}^{RELAB}(i = 30^\circ, e = 0^\circ, \lambda)$ is the absolute Spectralon REFF value measured by RELAB (Yang et al., 2019). Although the RELAB spectra

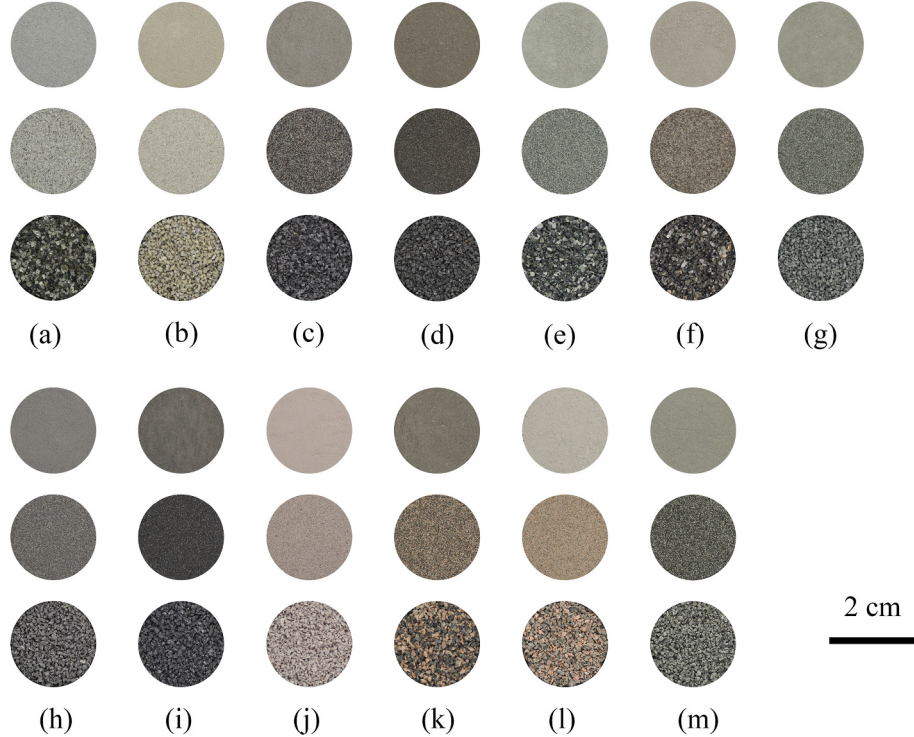


Fig. 3. Photos of the powdered rock samples with 3 size fractions: (a) Dunite; (b) Peridotite; (c) Olivine pyroxenolite; (d) Picrite porphyrite; (e) Kimberlite; (f) Gabbro; (g) Diabase; (h) Olivine basalt; (i) Andesite basalt; (j) Trachyte; (k) Pyroxenite syenite; (l) Orthophyre; (m) Lamprophyre. For each sample, the upper, middle and lower pictures correspond to the size distribution of 0–45 µm (Size 1), 90–125 µm (Size 2), 450–900 µm (Size 3), respectively.

Table 1
Rock samples with brief descriptions.

Igneous rock	Location	Description
Dunite	Jiande, Zhejiang Province, China	Composed almost entirely of olivine (90 ~ 100%), dense and hard
Peridotite	Xixia, Henan Province, China	Mainly composed of olivine and pyroxene. The content of olivine is 40%–90%.
Olivine pyroxenolite	Shandong Province, China	A rock between pyroxene and peridotite. It is composed of pyroxene and olivine, the content of pyroxene is 60% ~ 95%.
Picrite porphyrite	Jinyun, Zhejiang Province, China	It is mainly composed of pyroxene and olivine, and with a small amount of plagioclase. The phenocrysts are serpentinized olivine and augite
Kimberlite	Mengyin, Shandong Province, China	Serpentinized porphyritic phlogopite peridotite.
Gabbro	Jinan, Shandong Province, China	The main mineral composition is plagioclase and clinopyroxene, and auxiliary minerals are olivine, orthopyroxene, amphibole, biotite, and contain a small amount of potassium feldspar and quartz.
Diabase	Deqing, Zhejiang Province, China	The main mineral composition is pyroxene and basic plagioclase, and contains a small amount of olivine, biotite, quartz, apatite, magnetite, ilmenite, etc.
Olivine basalt	Luhe, Jiangsu Province, China	The main minerals are plagioclase, pyroxene, and olivine.
Andesite basalt	Zhuji, Zhejiang Province, China	It is mainly composed of basic feldspar, pyroxene, olivine, amphibole and biotite and is serpentinized.
Trachyte	Lingyuan, Liaoning Province, China	The mineral composition of trachyte is mainly composed of potassium feldspar, and it contains a small amount of plagioclase and mafic minerals. The mafic minerals are mainly amphibole, biotite and a small amount of pyroxene
Pyroxenite syenite	Shanxi Province, China	It is mainly composed of feldspar, hornblende, and biotite.
Orthophyre	Deqing, Zhejiang Province, China	It is mainly composed of feldspar, amphibole and biotite
Lamprophyre	Zaozhuang, Shandong Province, China	The main minerals are olivine, pyroxene, amphibole, and biotite.

were measured at $i = 30^\circ$ and $e = 0^\circ$, the reciprocity relation

$$REFF(i, e) = REFF(e, i), \quad (2)$$

ensures they are equivalent to $REFF(0^\circ, 30^\circ)$ (Hapke, 2012). Measurements made using our spectro-goniometer have a maximum deviation from reciprocity about 1.5%, indicating the good quality of the data.

For measurements on slab samples, we performed at least three measurements at different regions of the slab surface and used their average as the slab spectra. This would reduce the effects of surface material heterogeneities as some igneous rocks have porphyritic textures that contain centimeter-sized minerals. For measurements on powders, we first poured the grains into the sample holder and moved a ruler along different directions to make a flat surface. To reduce any surface inhomogeneities, measurements were made along two perpendicular directions and their average was used as the spectra of powders. It was found that the relative difference between the two perpendicular directions is within 2% in spectral ranges 0.35–0.45 μm and 0.9–1.15 μm , and is less than 0.5% elsewhere. The distance from the sample surface to the light source and the detector remained unchanged for all measurements.

2.3. Data processing

Since the spectra of some samples are noisy at the boundary between

Table 2
Chemical compositions in wt% of the 13 rocks. LOI: loss on ignition. TFe₂O₃ stands for the total of FeO and Fe₂O₃. Mg#: molar Mg/(Mg + Fe) × 100.

Major element	Dunite	Peridotite	Olivine pyroxenolite	Picrite porphyrite	Kimberlite	Gabbro	Diabase	Olivine basalt	Andesite basalt	Trachyte	Pyroxenite syenite	Orthophyre	Lamprophyre
SiO ₂	44.140	42.700	46.940	45.680	35.330	51.430	45.500	47.850	44.600	73.400	48.620	67.110	52.630
Al ₂ O ₃	1.950	0.740	13.200	11.690	3.940	14.190	15.810	14.720	12.300	14.690	14.880	11.930	
TFe ₂ O ₃	8.630	8.590	11.440	12.590	7.240	9.090	12.680	11.610	13.940	2.260	11.510	3.270	7.830
MgO	42.260	46.440	9.230	10.610	29.780	9.310	6.770	10.410	8.530	0.200	4.630	0.790	12.380
CaO	1.700	0.800	9.470	9.390	6.270	9.210	6.410	7.700	9.350	0.480	7.760	1.770	5.370
Na ₂ O	0.150	0.047	3.240	2.420	0.043	2.610	2.230	3.250	3.710	2.920	4.320	2.980	4.270
K ₂ O	0.042	0.015	2.010	1.210	1.640	1.330	1.660	1.630	0.870	5.090	1.580	5.030	0.190
TiO ₂	0.081	0.016	1.850	2.290	0.950	0.560	1.160	1.930	2.500	0.190	2.870	0.420	0.420
P ₂ O ₅	0.007	0.005	0.540	0.580	0.180	0.240	0.940	0.350	0.770	0.009	0.780	0.140	0.160
MnO	0.120	0.120	0.160	0.170	0.110	0.140	0.190	0.160	0.170	0.014	0.180	0.066	0.110
H ₂ O	0.060	0.060	0.100	0.660	0.400	0.120	0.240	0.000	0.520	0.900	0.120	0.200	0.820
LOI	0.240	0.580	0.360	2.700	12.780	0.340	4.940	-0.720	1.800	2.440	1.840	2.400	4.180
Total	99.32	100.05	98.44	99.33	98.26	98.45	98.29	98.89	98.32	99.30	98.78	98.86	99.47
Mg#	90.66	91.47	61.53	62.56	89.08	67.01	51.42	64.00	54.82	14.93	44.37	32.39	75.82

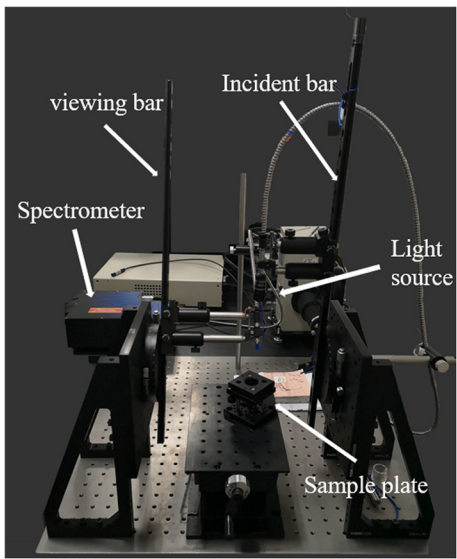


Fig. 4. The bi-directional reflectance spectrometer system used in reflectance measurement.

the silicon and InGaAs detectors of the SR-2500 spectrometer ($1.1\text{ }\mu\text{m}$), we used the Savitzky-Golay algorithm to smooth the spectra without changing the spectral shape and the absorption positions. We also removed the data above wavelength $2.4\text{ }\mu\text{m}$ due to their lower signal-to-noise values.

To extract the spectral information for quantitative analysis, we calculated the band depth, the full-width at half maximum (FWHM), and the band area of the samples as follows. The band depth can be estimated as

$$BD = 1 - \frac{BC_{REFF}}{BC_{continuum}}, \quad (3)$$

where BC_{REFF} is the reflectance at the band center, and $BC_{continuum}$ is the reflectance of the continuum at the band center (Clark and Roush, 1984; Dunn et al., 2010). The band center was chosen as the minimum point of the band in the continuum-removed spectra. The continuum was approximated by straight-line segments and the continuum-removed spectra have reflectance value of 1 on the both sides of the $1\text{ }\mu\text{m}$ absorption (Figure S1). For continuum-removed spectra, equation (3) can be simplified as

$$BD = 1 - BC_{crREFF}, \quad (4)$$

where BC_{crREFF} is the band center reflectance value of the continuum-removed spectra, which is slightly different from BC_{REFF} . The FWHM of an absorption band is the full width at half depth in the continuum-removed spectra. As a measure of the absorption intensity, the band area was calculated as the area between the $1\text{ }\mu\text{m}$ band curve and the continuum line.

3. Measurement results

3.1. Particle size and brightness

Fig. 5 and **Fig. 6** show the original and normalized reflectance spectra of the 13 igneous rocks and their powders in three size fractions. In contrast to their slab counterparts, most powdery samples have a pronounced absorption feature around $1\text{ }\mu\text{m}$, and whether the slabs have pronounced absorption features is related to their reflectance values. If the slab samples' reflectance value at $0.5\text{ }\mu\text{m}$ $REFF(0.5\mu\text{m})$ is used to represent the surface brightness (reflectance at $0.5\text{ }\mu\text{m}$ is not affected by the $1\text{ }\mu\text{m}$ absorption), these samples may be roughly classified into two

groups according to their different slab-powder spectral feature relations: for those with a $REFF(0.5\mu\text{m})$ value smaller than 0.1, the spectra of their slabs are quite blue (decreased reflectance with increased wavelength) compared to their powders' spectra, and show less pronounced absorption features (Dunite, Olivine pyroxenolite, Picrite porphyrite, Kimberlite, Gabbro, Olivine basalt). Although the $REFF(0.5\mu\text{m})$ of Dunite is slightly larger than 0.1, the spectrum of its slab has less pronounced absorption features, and thus this sample is classified as this group. For those with a $REFF(0.5\mu\text{m})$ value larger than 0.1, the spectra of their slabs have a neutral slope and show absorption features consistent with their powders' spectra (Peridotite, Diabase, Trachyte, Pyroxene syenite, Orthophyre, and Lamprophyre). The only exception is Andesite basalt, which has a $REFF(0.5\mu\text{m})$ value smaller than 0.1 and weak $1\text{ }\mu\text{m}$ absorption features for Size 2 and Size 3, yet its slab spectrum has pronounced absorption features. By performing micro-Raman measurements on Andesite basalt, we found that it was fairly easy to find serpentine's Raman fingerprint peaks in the slab sample, but it was very difficult to find that in the powders. Although a few other samples also have the hydration features at $\sim 1.4\text{ }\mu\text{m}$, $1.9\text{ }\mu\text{m}$, and $2.3\text{ }\mu\text{m}$ (e.g., Kimberlite and Trachyte), their slab-powder spectral relationships do not show such an "abnormal" behavior. Overall, the presence of these smaller hydrous mineral peaks does not affect the overall $1\text{ }\mu\text{m}$ spectral feature links between the slabs and powders for samples except for Andesite basalt. A thorough understanding of the unusual behavior of the Andesite basalt will need a future investigation.

Fig. 7 displays the average reflectance (the average of reflectance values at all wavelengths) and the spectral slope around $1\text{ }\mu\text{m}$ from 0.35 to $1.5\text{ }\mu\text{m}$, normalized to the value of Size 1, for all samples. Since many samples have a very red slope, the reflectance value at a single wavelength (e.g., $REFF(0.5\mu\text{m})$) may be insufficient to represent the sample brightness at all wavelengths. Therefore, we used the average reflectance over the full wavelength range to look at the brightness-spectral slope relationship. We chose 0.35– $1.5\text{ }\mu\text{m}$ as the slope calculation range for the $1\text{ }\mu\text{m}$ absorption peak to reduce any possible influence of the $2\text{ }\mu\text{m}$ absorption. The spectral slope for each spectrum shown in **Fig. 5** is approximated by the slope of a straight line connecting the average of the first 10 data points and the average of the last 10 data points. We used the 10-point average to reduce the effect of the noise, as the data have larger uncertainties at the edges of the spectra, especially at the shortest and longest wavelengths. Both the average $REFF$ and spectral slope plots have been divided into two groups according to their corresponding slab samples' $REFF(0.5\mu\text{m})$ values, i.e., those larger than 0.1 and those smaller than 0.1. In general, when a rock is pulverized, its powder would have a higher surface albedo because of the higher single scattering albedo of smaller particles and the strong multiple scattering between them (e.g., Bohren, 1987; Harloff and Arnold, 2001; Carli and Sgavetti, 2011; Paton et al., 2011). In **Fig. 7**, the "the coarser the darker" (or "the finer the brighter") rule appears valid from Size 1 to Size 3 for all samples except for Andesite basalt whose Size 2 and Size 3 have similar brightness. This exception may be caused by some complex factors, e.g., the presence of opaque minerals in the sample (e.g., Riner et al., 2009), and would merit further investigations in the future. **Fig. 7** shows that the average reflectance value of Size 3 is comparable to Size 4 for most samples, and in a few cases, there is an observable change in the spectrum of Size 3 and Size 4 (e.g., Kimberlite, peridotite and Diabase). The reflectance spectral properties of Size 3 (450–900 μm) are close to those of slabs (Size 4), indicating that the particle size dependence is weakened at larger particle sizes (greater than Size 3). Thus, it is likely that the reflectance spectroscopic properties of Size 3 (450–900 μm) are already close to that of the slabs (Size 4) for these samples. This is similar to the finding of Adams and Filice (1967) that particles larger than 500 μm have similar albedos. By estimating the thickness that controls the amount of light reflected from a particulate layer (Hapke, 2012), we found that, for Size 1 to Size 3, the penetration depths are about a few particle layers for most samples (Text S2, Figures S2 and S3), consistent with laboratory measurement results (Zhang et al., 2003). The unusually

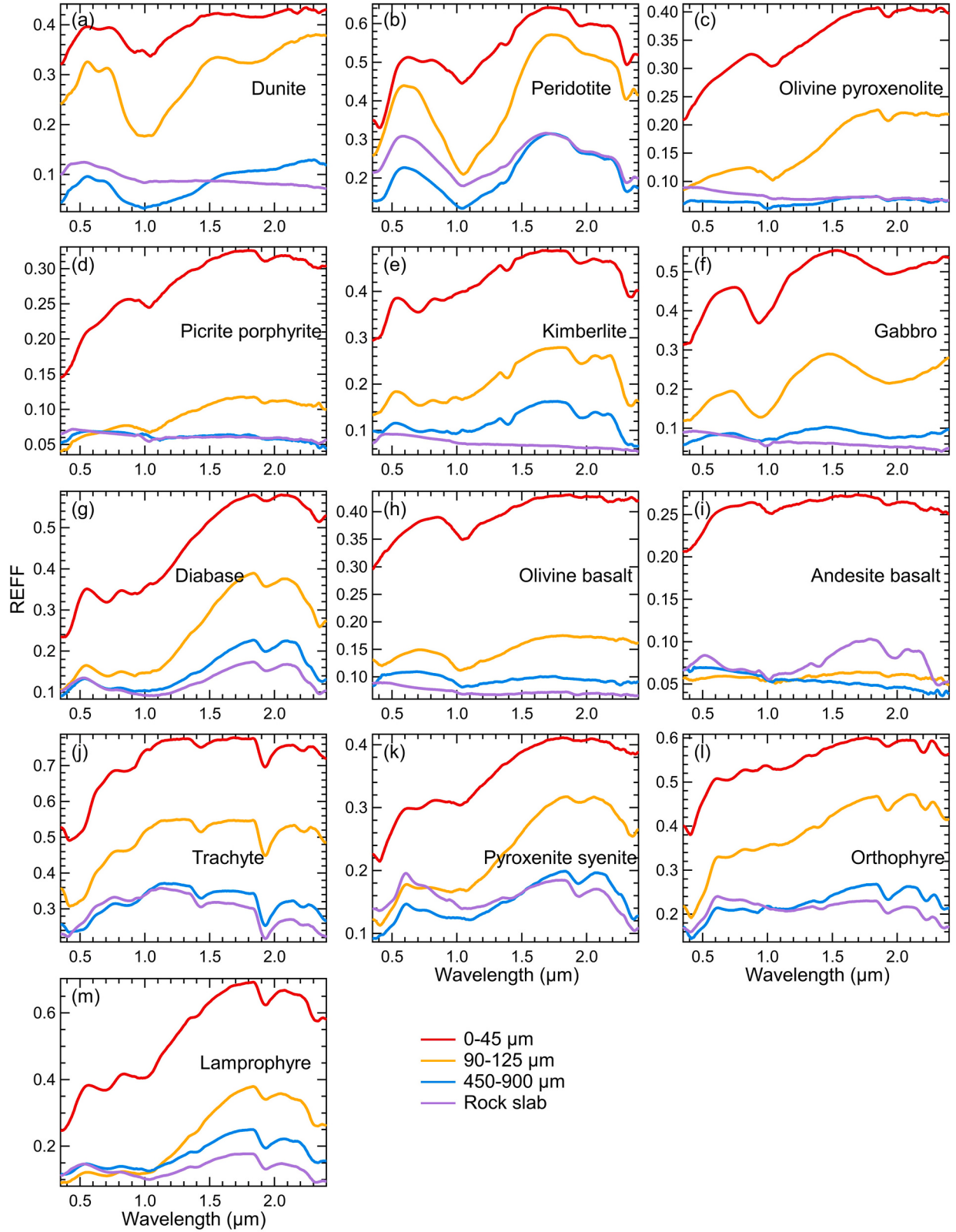


Fig. 5. Reflectance spectra of the 13 igneous rocks and their powders in 3 size fractions. All measurements were made at $i = 0^\circ$, $e = 30^\circ$.

large penetration depth values for Size 4 (~cm-sized) may be attributed to the failure of the model when applied to the slab sample.

Fig. 7 also shows that, the normalized 1 μm spectral slope generally decreases monotonically with increasing particle size, except for Andesite basalt, Orthopyre, and Trachyte. For samples with a slab REFF

(0.5 μm) value larger than 0.1 (samples whose slabs have pronounced 1 μm absorption features), their slabs (Size 4) have positive normalized spectral slopes (Fig. 7d), while those with a slab REFF(0.5 μm) value smaller than 0.1 (samples whose slabs have less pronounced 1 μm feature), their slabs (Size 4) have negative normalized spectral slopes,

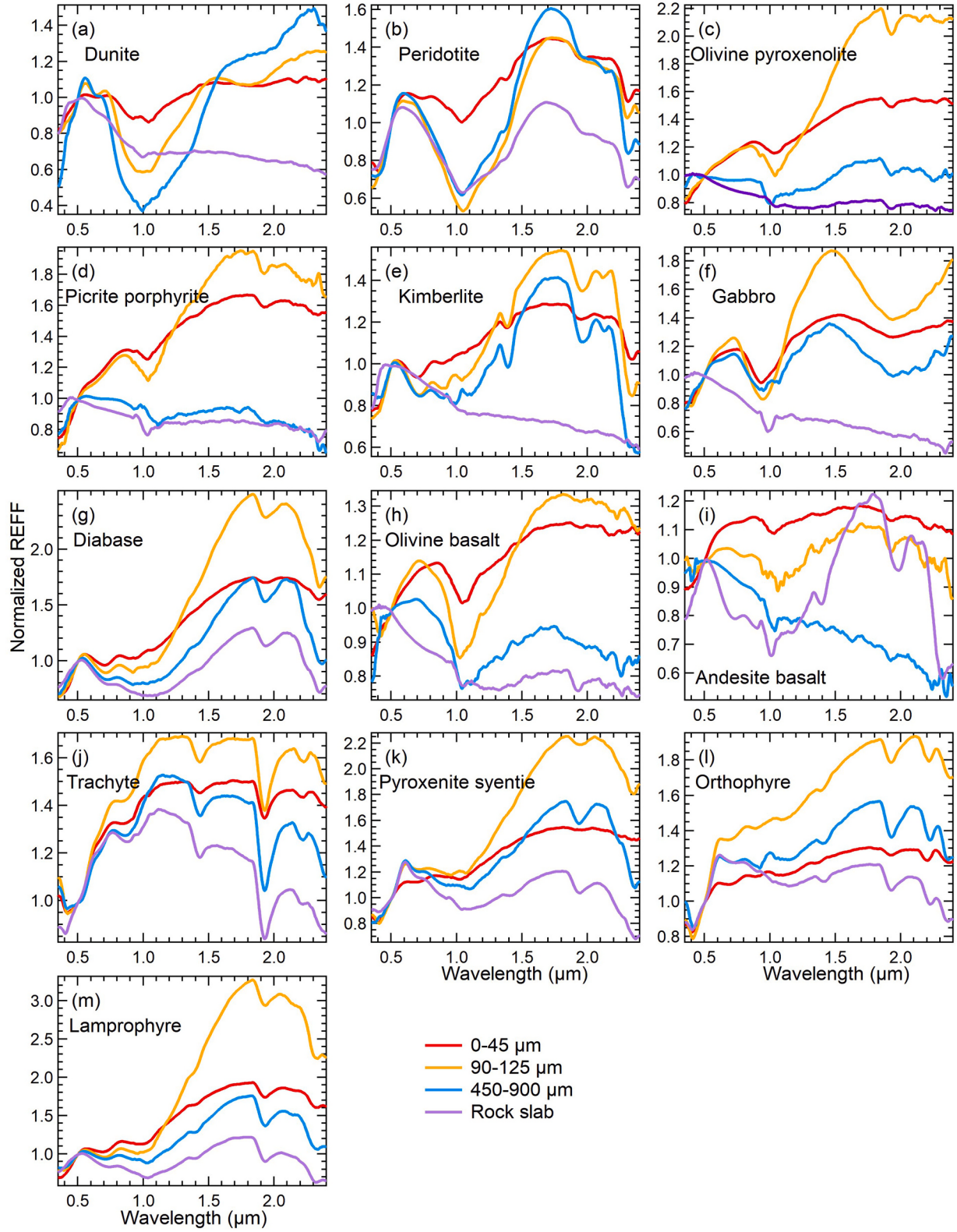


Fig. 6. Same as Fig. 5, but normalized at 0.5 μm for all spectra.

except for Andesite basalt (Fig. 7c). The VNIR spectral slope decrease from smaller to larger grains has long been observed experimentally (e.g., Adams and Filice, 1967) and its quantitative explanation would merit further investigations.

3.2. The 1- μm band absorption features

Fig. 8 shows the continuum removed spectra for all samples, with the vertical lines indicating the band centers of the 1 μm absorption. Although particles with different size distributions have different band depths, the band positions remain largely unchanged. For samples with

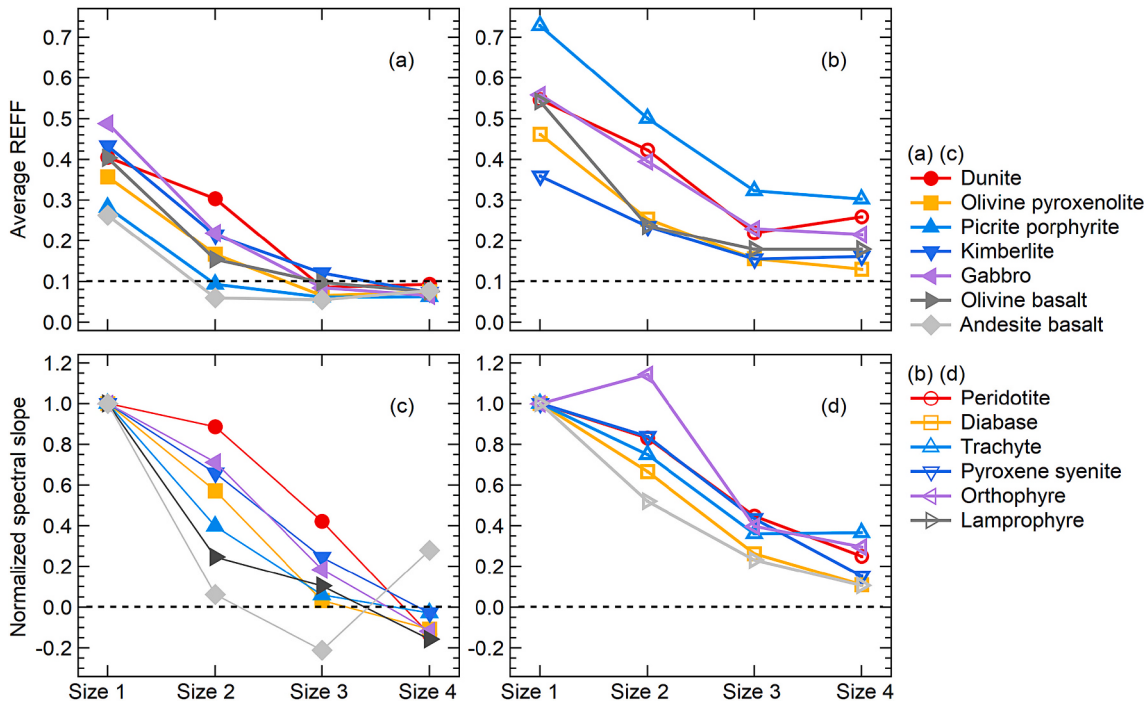


Fig. 7. The dependence of the average $REFF$ and normalized spectral slope around the $1\text{ }\mu\text{m}$ absorption ($0.35\text{--}1.5\text{ }\mu\text{m}$) on particle size. Samples in (a) and (c) have $REFF(0.5\text{ }\mu\text{m})$ values smaller than 0.1 and those in (b) and (d) have $REFF(0.5\text{ }\mu\text{m})$ values larger than 0.1. Size 1 to Size 4 correspond to $0\text{--}45\text{ }\mu\text{m}$, $90\text{--}125\text{ }\mu\text{m}$, $450\text{--}900\text{ }\mu\text{m}$, and rock slab, respectively.

slightly shifted band centers, their $1\text{ }\mu\text{m}$ bands consist of smaller absorption features (e.g., Kimberlite) whose positions may change after continuum removal. However, this would not change the overall trend of the $1\text{ }\mu\text{m}$ absorption feature from powders to slabs.

Fig. 9 shows the dependence of the $1\text{-}\mu\text{m}$ band depth, FWHM, and band area on different particle sizes for all samples. For clarity, these parameters have been normalized to that of the Size 1 (for an un-normalized version, see Figure S4)). Similar to Fig. 7, the plots in Fig. 9 have been divided into two groups according to whether their $REFF(0.5\text{ }\mu\text{m})$ values are smaller ((a), (c), (e)) or larger than 0.1 ((b), (d), (f)). For band depth and band area, the first group undergoes a rapid growth from Size 1 to Size 2 (or Size 3 for Dunite and Kimberlite), and then decreases from Size 2 (Size 3) to Size 4. In contrast, for most samples in the second group, after a rapid growth from Size 1 to Size 2 (Size 3 for Orthopyre), the band depth and band area plateau out. For FWHM, most samples in the second group show a steady increase from Size 1 to Size 4 while most samples in the first group show a decrease from Size 3 to Size 4. It should be noted that, the sharp increase of the $1\text{-}\mu\text{m}$ absorption depth from Size 1 to Size 2 was not caused by compositional difference. Instead, it was caused by the scattering property change from very fine to larger grains, both observed by previous researchers (e.g., Harloff and Arnold, 2001; Hapke, 2012) and is present in model spectra (Figure S5). It should be noted that the non-monotonous change of the absorption depth (or band contrast) with grain size has been observed in laboratory spectra (Figure S6) and can be demonstrated by model calculations as well (Figure S7).

3.3. Comparisons of reflectance spectra on natural and cut surfaces

Since the natural surfaces of the intact rocks are very irregular, rough, and different rock surfaces have different degrees of roughness, we cut and slightly polished the rocks to equalize the surface condition as much as possible. In order to look at the effects of cutting, we measured the reflectance spectra of the natural surfaces and the cut (and then slightly polished) ones of four selected rocks, Dunite, Olivine pyroxenolite, Kimberlite, and Olivine basalt. These samples were

selected because their original rocks showed no signs of weathering. Figure S8 shows the comparison results and one can see that the reflectance spectra of the natural and cut surfaces have similar spectral features, but very different absolute $REFF$ values caused by uneven illumination and shadows in a natural surface. As all reflectance measurements were carried out at a non-specular configuration (incident zenith 0° and viewing zenith 30°), any possible specular reflection effect for the polished surfaces can be safely excluded.

4. A model study using the equivalent slab model and the Hapke model

The above results show that the spectral features of the 13 samples can be roughly divided into two groups with distinct spectral features, depending on whether their slab samples have a pronounced $1\text{ }\mu\text{m}$ absorption feature. Since these two groups have distinct surface albedos with their $REFF(0.5\text{ }\mu\text{m})$ values higher or lower than 0.1, it is natural to wonder if such a dichotomy can be explained by reflectance modelling. To look at this, we derived the optical constants of the samples using the Equivalent-slab model (for single scattering) and the Hapke model (for multiple scattering) (e.g., Hapke, 2012; Lucey, 1998; Sun and Lucey, 2021) and studied the contributions from surface scattering.

4.1. Model descriptions

For many silicate materials, the real refractive index n in the visible and near-infrared is between 1.5 and 1.8 and does not change rapidly with wavelength and can be approximated as constant (~ 1.6) in spectroscopic modeling (e.g., Hiroi and Pieters, 1994; Lucey, 1998). The prominent absorption features in the VNIR are mostly controlled by imaginary refractive index k and thus we can easily link the optical constants to single scattering albedo (SSA) and reflectance using the equivalent slab formulation and Hapke radiative transfer model (Lucey, 1998; Hapke, 2012; Sun and Lucey, 2021). In this approach, the SSA (ω) is related to k through the following equations:

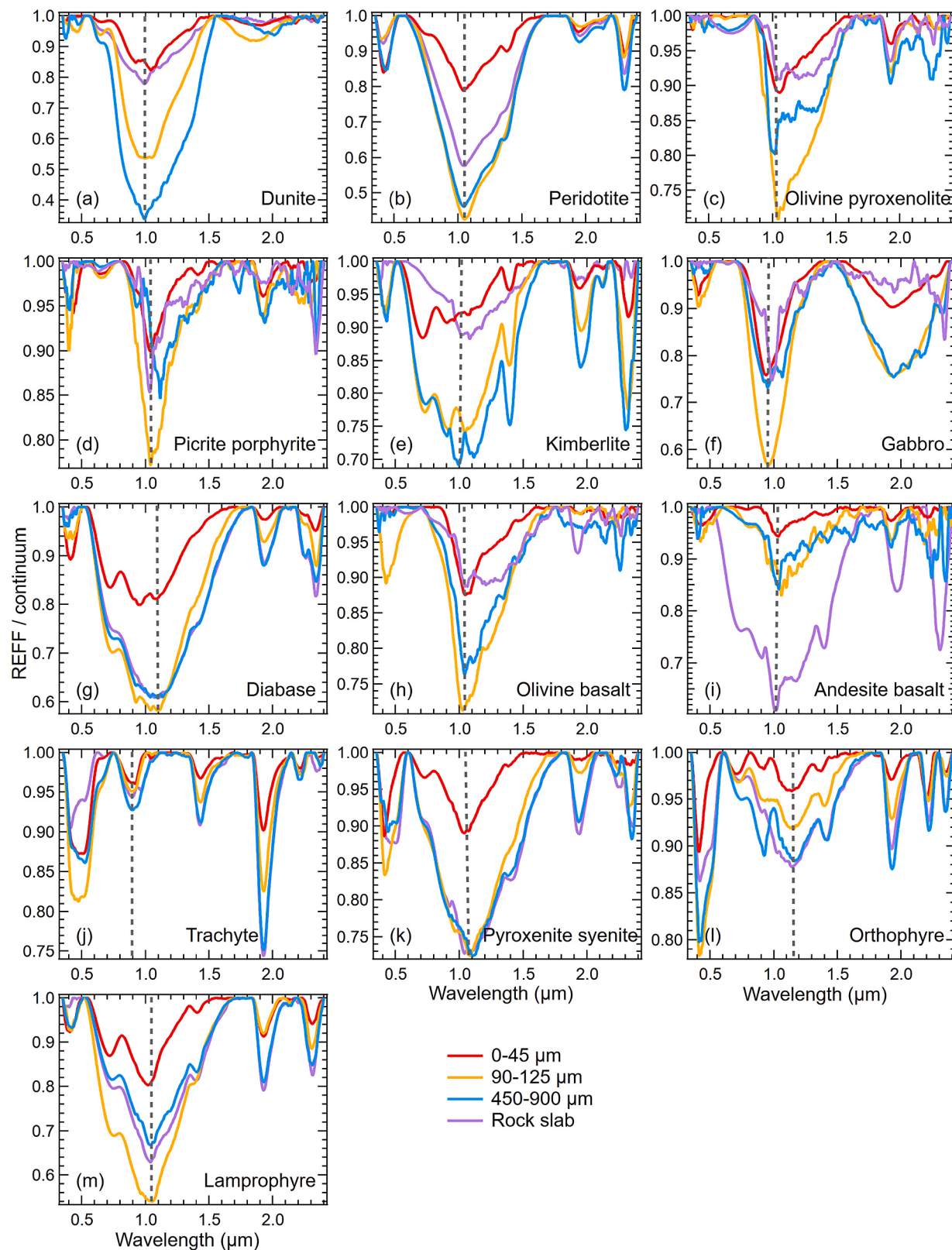


Fig. 8. Same as Fig. 5, but with the continua removed. The vertical dashed lines indicate the locations of the band centers.

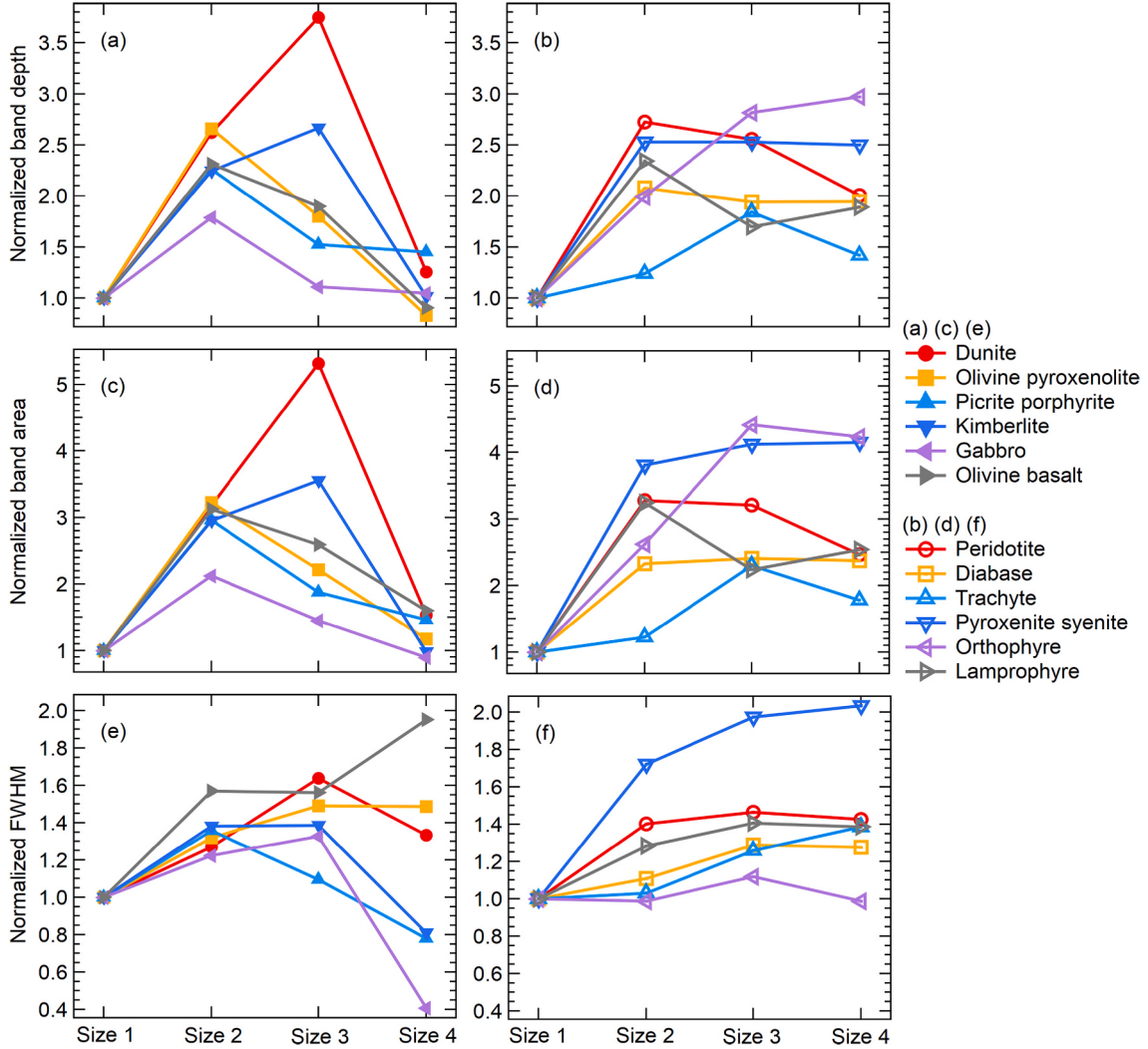


Fig. 9. The dependence of normalized band depth (a-b), band area (c-d), and the FWHM (e-f) of the 1 μm absorption for samples on particle size. Plots have been divided into two groups according to whether their $REFF(0.5\mu\text{m})$ values are smaller ((a), (c), (e)) or larger than 0.1 ((b), (d), (f)). Andesite basalt is not shown here for its lack of absorption features for most size fractions. Size 1 to Size 4 correspond to 0-45 μm, 90-125 μm, 450-900 μm, and rock slab, respectively. The un-normalized version of this graph is shown in Figure S4.

$$\omega = S_e + (1 - S_e)(1 - S_i) \frac{\Theta}{1 - S_i \Theta}, \quad (5)$$

where S_e and S_i are the surface reflection coefficients for light that is incident externally and internally, respectively, and Θ is the internal-transmission factor. S_e , S_i , and Θ are estimated by

$$S_e = \frac{(n - 1)^2}{(n + 1)^2} + 0.05, \quad (6)$$

$$S_i = 1.014 - \frac{4}{n(n + 1)^2}, \quad (7)$$

$$\Theta = \frac{r_i + \exp[-\sqrt{\alpha(\alpha + s)} \langle D \rangle]}{1 + r_i \exp[-\sqrt{\alpha(\alpha + s)} \langle D \rangle]}, \quad (8)$$

where s is the internal scattering coefficient, α is the wavelength-dependent absorption coefficient,

$$\alpha = \frac{4\pi k}{\lambda} \quad (9)$$

$\langle D \rangle$ is the effective particle size and is related to physical size D as

$$\langle D \rangle = \frac{2}{3} \left[n^2 - \frac{1}{n} (n^2 - 1)^{\frac{3}{2}} \right] D \quad (10)$$

and

$$r_i = \frac{1 - \sqrt{\alpha/(\alpha + s)}}{1 + \sqrt{\alpha/(\alpha + s)}} \quad (11)$$

The $REFF$ can then be obtained as

$$REFF(i, e, g) = \frac{1}{4} \frac{\omega}{\mu_0 + \mu} [p(g) + H(\mu_0)H(\mu) - 1], \quad (12)$$

where μ_0 and μ are respectively the cosines of the incident and viewing zenith angles, g is the phase angle, $p(g)$ is the single particle phase function and can be approximated by an empirical two-term Legendre polynomial as

$$p(g) = 1 + b \cos(g) + c(1.5 \cos^2(g) - 0.5), \quad (13)$$

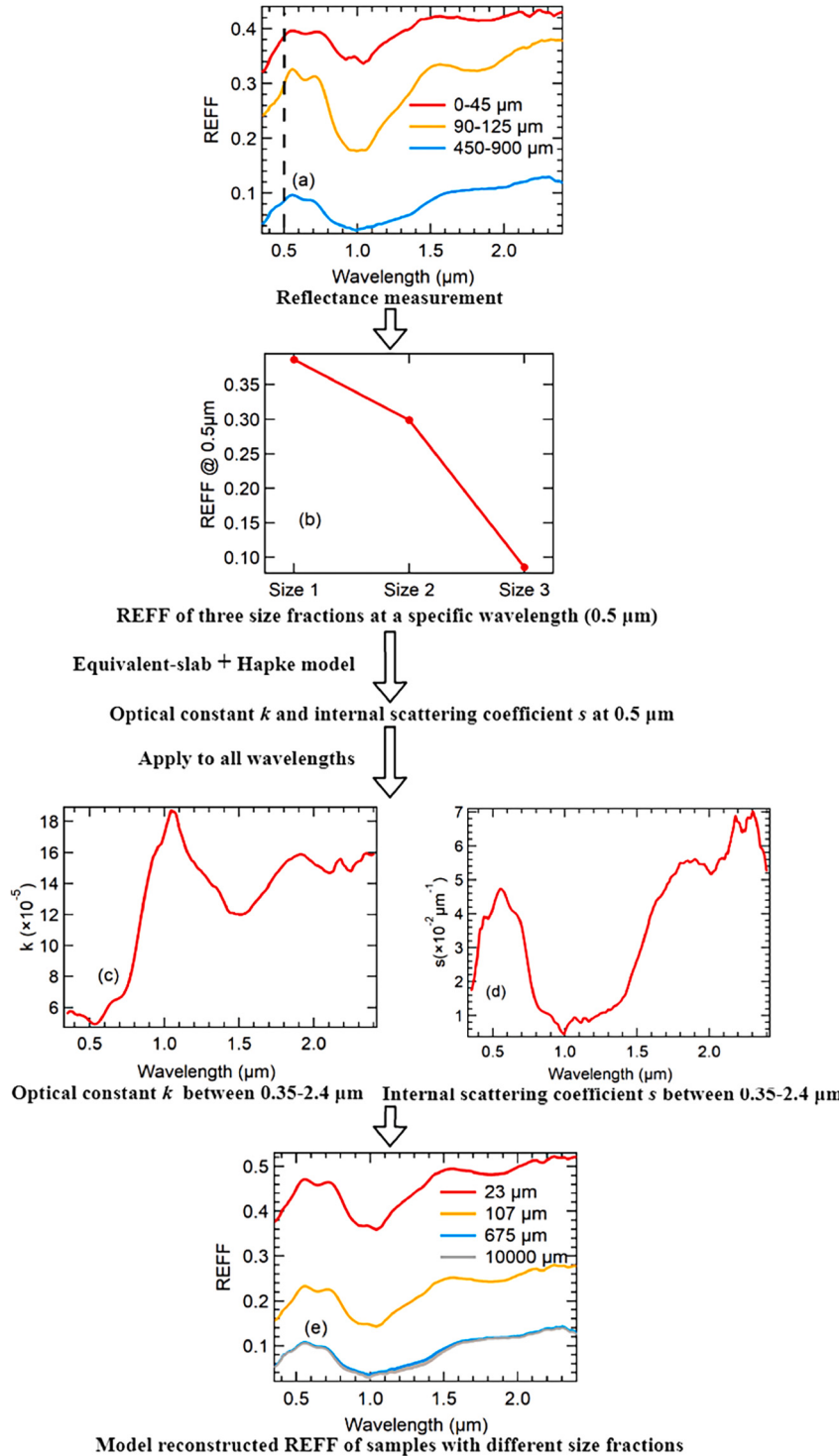
where $b = -0.4$ and $c = 0.25$ are constants that determine the shape of the phase function (Mustard and Hays, 1997; Lucey, 1998). The H function in equation (12) can be approximated by (Hapke, 2002)

$$H(x) = \left[1 - \omega x \left(r_0 + \frac{1 - 2r_0x}{2} \ln \frac{1+x}{x} \right) \right]^{-1}, \quad (14)$$

where

$$r_0 = \frac{2}{1 + \sqrt{1 - \omega}} - 1. \quad (15)$$

To be consistent with our measurement geometry (Section 2.2), the incident and viewing zenith angles were fixed to be 0° and 30° , respectively.



With the above formulations and the assumption that $n = 1.6$ at all wavelengths (the effect of varying n is shown in Text S6 and Figure S9), we can calculate the $REFF$ of minerals and rocks if their optical constants k , internal scattering coefficient s , and particle size D are given. Since we have measured the spectra of samples with three known size fractions, we can use equations. (5)-(15) to fit the measured $REFF$ to obtain the imaginary refractive index k and internal scattering coefficient s of the samples. Then, we can use the fitted k and s values to calculate the spectra of the samples with different particle sizes. Using Dunite as an example, we illustrate the procedure in Fig. 10. Starting with the $REFF$

Fig. 10. Flow chart to illustrate the procedure to infer the imaginary refractive index k and internal scattering coefficient s , and reconstruct the model spectra, using Dunite as an example. (a) Measured reflectance spectra of three size fractions, 0-45 μm (Size 1), 90-125 μm (Size 2), and 450-900 μm (Size 3). The vertical dashed line indicates the wavelength 0.5 μm . (b) Measured $REFF$ at 0.5 μm versus three sizes; the particle size D used in the fitting are 23 μm for Size 1, 107 μm for Size 2, and 675 μm for Size 3; by fitting the measurement to the equivalent-slab + Hapke model, the k and s values at wavelength 0.5 μm are obtained. (c) and (d) are the fitted k and s values over the full wavelength region, respectively. (e) Model reconstructed spectra for powders with three size fractions and for the slab samples by using the fitted k and s values. The D value for the slab sample was tentatively set to be 10000 μm .

spectra (Fig. 10a) of three size fractions (Size 1, Size 2, and Size 3), we fit the model to measured $REFF$ versus sizes (parameter D in equation (10)) at each specific wavelength to obtain k and s (Fig. 10b). We used the average of the maximum and minimum values of each particle size

fraction to represent its parameter D and substitute them into the model for calculation (i.e., Size 1 is represented by $D = 23 \mu\text{m}$, Size 2 is represented by $D = 107 \mu\text{m}$, and Size 3 is represented by $D = 675 \mu\text{m}$). After the spectral k values (Fig. 10c) and s values (Fig. 10d) from 0.35 to 2.4

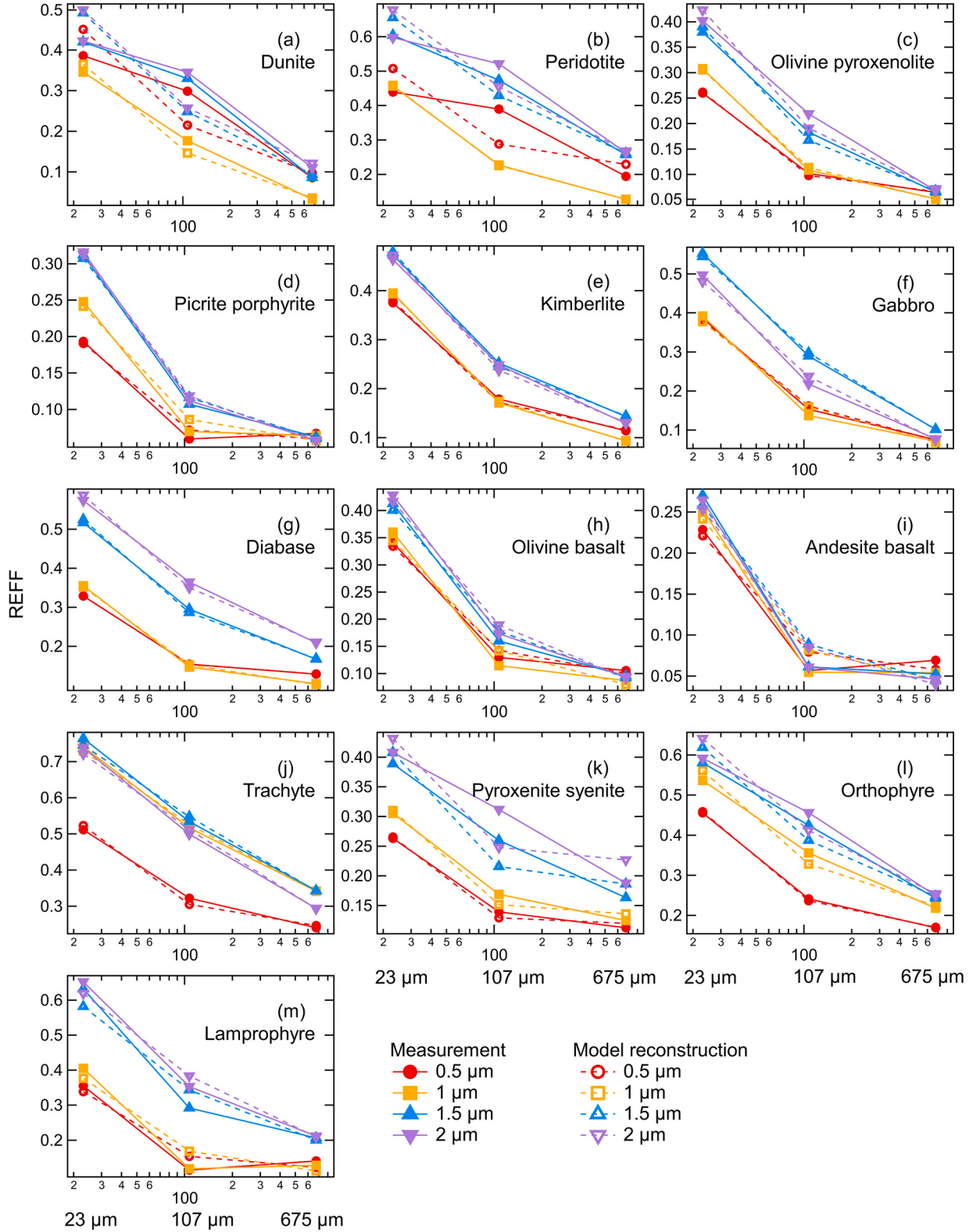


Fig. 11. Comparisons of measurement and model (equivalent-slab + Hapke) reconstructed spectra at four wavelengths, 0.5 μm , 1.0 μm , 1.5 μm , and 2.0 μm for all 13 samples. The coordinate for each plot is particle size D in equation (10), and the averages of the three size fractions are shown in the bottom three plots, i.e., 23 μm for Size 1, 107 μm for Size 2, and 675 μm for Size 3.

μm are obtained, we can predict the spectra of the slab samples by assuming a very large grain size, $10000 \mu\text{m}$ (Fig. 10e). It should be noted that the use of such a large grain size is just a stopgap due to the lack of a rock reflectance model. The advantage of using three particle sizes for optical constant retrieval is that the fitted values can better represent the optical properties of the material in all size fractions, rather than being potentially biased towards a specific particle size. We also tried a model without the internal scattering coefficient ($s=0$) and found the model reconstructed reflectance values of large-sized particles are much lower than measurement, especially in the visible region (Figure S10). Therefore, keeping s as a model parameter makes more sense. The retrieved imaginary refractive index (k) and the internal scattering coefficient (s) of all 13 samples are shown in Figure S11 and Figure S12.

4.2. Model fitting results

The $REFF$ versus particle size fitting results for all samples at 4 typical wavelengths, $0.5 \mu\text{m}$, $1.0 \mu\text{m}$, $1.5 \mu\text{m}$, and $2.0 \mu\text{m}$, are shown in Fig. 11, and the model reconstructed spectra using the fitted k and s values are shown in Fig. 12. The results shown in Figs. 11 and 12 indicate that, although the model fitting did not produce perfect model reconstructed spectra for all samples and all size fractions, the results are reasonably satisfactory for most samples, especially considering the model simplicity and our crude assumption that all samples have a constant n value (1.6) in the full wavelength region. Therefore, the optical constant k and internal scattering coefficient s obtained from the fitting may represent the optical properties of the samples rather well. The fitted curves (Fig. 12) show that when particle size D goes beyond $675 \mu\text{m}$, most model spectra do not change much. This should be mainly caused by the failure of the equivalent slab model when applied to very large grains ($D \sim$ hundreds of micrometers), as the measurement results show that, for most samples except for Picrite porphyrite, the reflectance spectra of rock slabs are different from that of the Size 3. It is also likely that when particle size reaches a certain value (hundreds of micrometers), the reflectance spectra of the particulate samples become close to that of the rock slabs.

The mismatch between the model reconstructed spectra and measurements in some samples could be caused by several factors. The fitting results shown in Fig. 11 show that, when measurement and fitting over three sizes have similar slopes (e.g., Olivine pyroxenolite, Picrite porphyrite, Kimberlite), the model spectra agree with the measurements well (Fig. 12). On the other hand, if measurement and fitting have opposite slopes (e.g., Dunite, Peridotite), the model spectra and measurements may differ significantly. By fitting equations (5)-(15) to measurements of three sizes to obtain k and s , the fitted values may be considered as the optimized parameters for all three sizes, but not necessarily the optimized values for each individual size. Therefore, when the fitted values are plugged into the model, the reconstructed spectra may be different from measurements of individual sizes. The use of an empirical particle single scattering phase function (equation (13)) and the negligence of the different filling factors for grains and slabs could also be a factor. Also, to model the reflectance of a rock slab, the equivalent slab model should be replaced by a realistic slab reflectance model similar to Hapke's diffusive reflectance model for slabs (Section 10.6.1.5 in (Hapke, 2012)). More modeling efforts are expected to accurately describe the realistic rock reflectance.

5. Discussion: effects of surface scattering contributions

Now we can look at the SSA dependence on the effective absorption thickness $\alpha\langle D \rangle$, the product of absorption coefficient and effective diameter of the samples, to understand the slab-powder spectral feature links. Specifically, we use equations (12)-(15) to compute the SSA from measured $REFF$, and calculate $\alpha\langle D \rangle$ for different sizes using the fitted k and s values. According to Hapke (2012), for $\alpha\langle D \rangle\langle D \rangle$ values between 0.01 and 100, a strong or weak SSA dependence on $\alpha\langle D \rangle$ would

indicate the reflectance is dominated by volume-scattering or weak surface-scattering, respectively. Specifically, as shown in Text S9 and Figure S13, when $\alpha\langle D \rangle$ is much smaller than ~ 1 , the interaction of light with the grain mainly occurs in the form of refraction, transmission, and scattering inside the grain. As $\alpha\langle D \rangle$ increases, the SSA decreases and when $\alpha\langle D \rangle$ exceeds ~ 1 in Figure S13, scattering is dominated by weak surface scattering and the SSA is independent of particle size, as long as $\alpha\langle D \rangle$ does not enter the strong surface scattering regime where $\alpha\langle D \rangle$ exceeds ~ 1000 . Figs. 13 and 14 show the dependence of the spectral SSA around the $1 \mu\text{m}$ absorption band versus $\alpha\langle D \rangle$ for our slab samples with pronounced and less pronounced absorption features, respectively. To avoid curve clutter caused by the dense data points, 20 data points at equal wavelength intervals in the $1 \mu\text{m}$ absorption region (~ 0.5 to $\sim 1.5 \mu\text{m}$) were selected from more than one thousand measured data points. The results for Andesite basalt are not shown here since its slab-powder $1 \mu\text{m}$ spectral link is an exception. Since the $\langle D \rangle$ value for an intact rock sample is unclear (i.e., a reflectance model for intact rock is unavailable), we tried to use very large particle sizes ($D = 10000 \mu\text{m}$) to represent the rock slabs. Again, the use of such a big D value for slabs is a stopgap measure due to the lack of a rock reflectance model and does not necessarily represent the actual value.

Since the spectra of all samples have varied mean reflectance (or SSA) and "dynamic range" (the maximum and minimum values), we did not unify the maximum and minimum ordinate values in Figs. 13 and 14, but instead plotted the graphs within their individual SSA ranges. Although the spectra shown in Figs. 13 and 14 are not as smooth and monotonic as the model spectrum shown in Figure S13, a comparison between Fig. 13 and 14 clearly shows the two groups have distinct behaviors: for almost all samples, spectra of Size 1, Size 2, and Size 3, are dominated by volume scattering, i.e., the SSA decreases steadily with the increase of $\alpha\langle D \rangle$. For rock slab samples with a pronounced $1 \mu\text{m}$ absorption feature (purples in Fig. 13), the variations in their SSA values are quite large (~ 0.2 , except for Trachyte and Orthophyre), implying volume scattering is dominant in the slab samples. In contrast, for slab samples with less pronounced $1 \mu\text{m}$ absorption feature (purples in Fig. 14), the SSA variations are quite small (~ 0.1), implying the scattering belongs to the weak surface-scattering region (Hapke, 2012). Note, "large" or "small" in variations are in a relative sense. In Fig. 13, the SSA variations of Trachyte (Fig. 13c) and Orthophyre (Fig. 13e) are smaller than that of the rest samples in this group, and are more commensurate with the samples shown in Fig. 14. This is consistent with the fact that these two samples' $1 \mu\text{m}$ features are weak in all size fractions.

From another perspective, since S_e (equation (6)) is the fraction of incident light specularly reflected into all directions from the grain surface, the ratio of S_e to SSA reflects the degree to which the spectrum is affected by surface scattering. The ratios of S_e to SSA for the two sample groups (except for Andesite basalt) are shown in Fig. 15 and Fig. 16, respectively. The ratios for slab samples shown in Fig. 15 are significantly lower than those in Fig. 16, indicating that for slab samples, volume scattering is more dominant in the first group while surface scattering is more dominant in the second group, consistent with the results shown Figs. 13 and 14. Note, since we equalized the n values for all samples ($n = 1.6$), comparisons of S_e/SSA are equivalent to comparisons of the inverse of the SSA values.

Light scattering modeling results (Hapke, 2012, Section 14.4) show that the absorption band depth is controlled by the absorption optical thickness $\alpha\langle D \rangle$ of the grain. In the volume scattering region, the absorption band has large band depth due to sufficient interaction between light and particles. However, in the weak surface scattering region, light is mainly reflected from the particle surface, which weakens the absorption feature. Therefore, the $1 \mu\text{m}$ absorption feature of darker slabs is not easily revealed in the reflectance spectra.

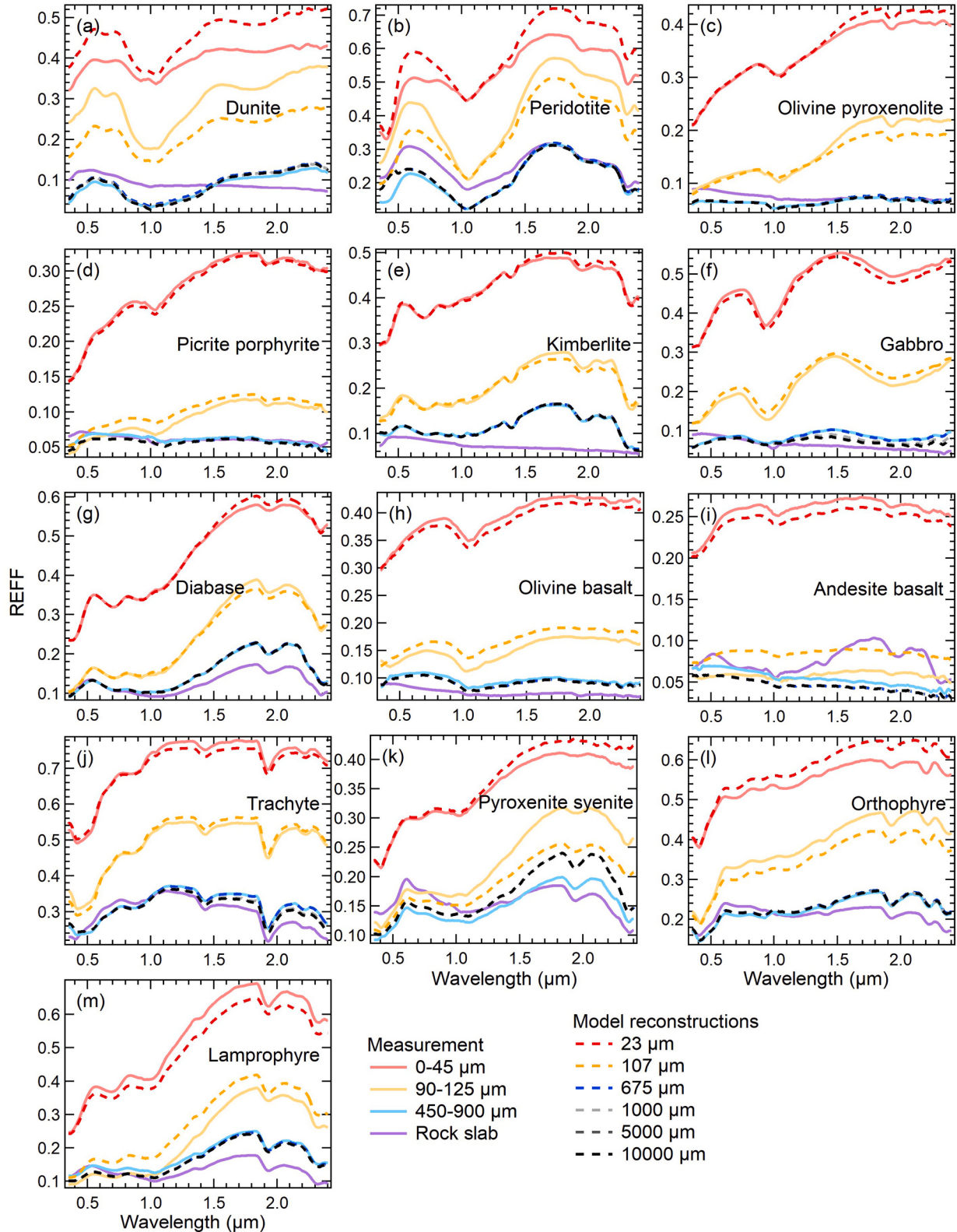


Fig. 12. Comparisons of measurement (solid lines) and model reconstructed spectra (dashed lines) for different size fractions for all samples. The model reconstructed spectra were obtained using the procedure outlined in Fig. 10. The model reconstructed spectra with particle sizes larger than 675 μm for some samples are too close to be distinguishable.

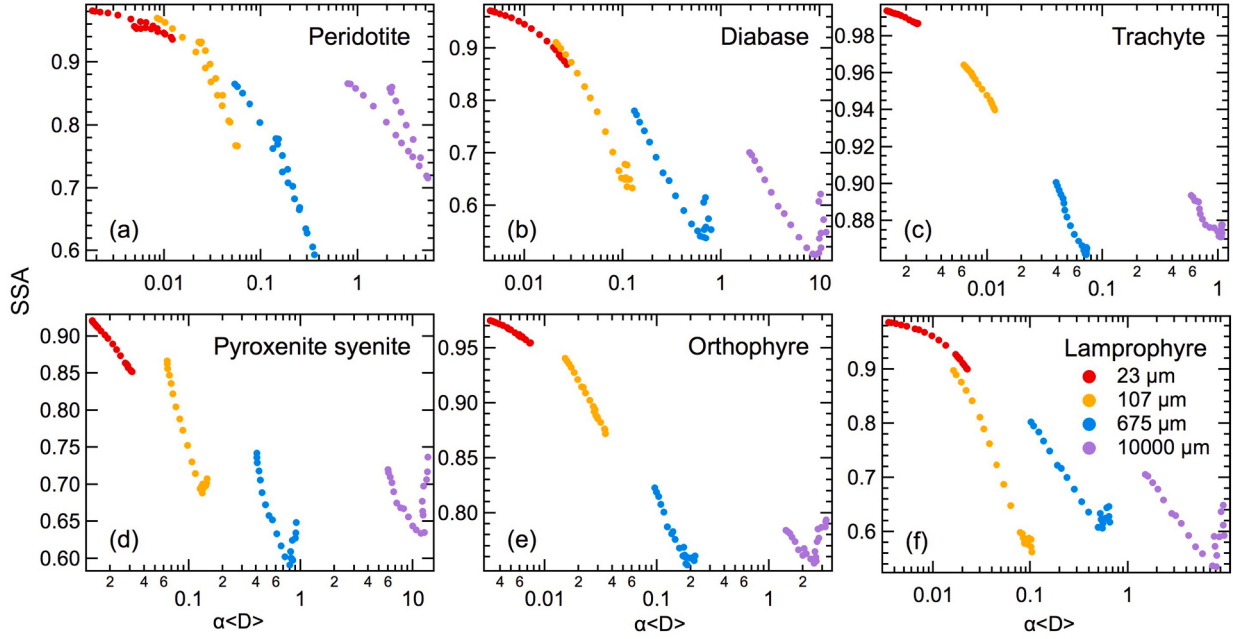


Fig. 13. The dependence of single scattering albedo (SSA) on effective absorption thickness $\alpha\langle D \rangle$ of the 1 μm absorption region (~ 0.5 to $\sim 1.5 \mu\text{m}$) for samples whose slabs have a pronounced 1 μm absorption feature. The four numbers shown in (f) are the average sizes for the three size fractions and the slab sample, Size 1, Size 2, Size 3, and the slab samples, respectively.

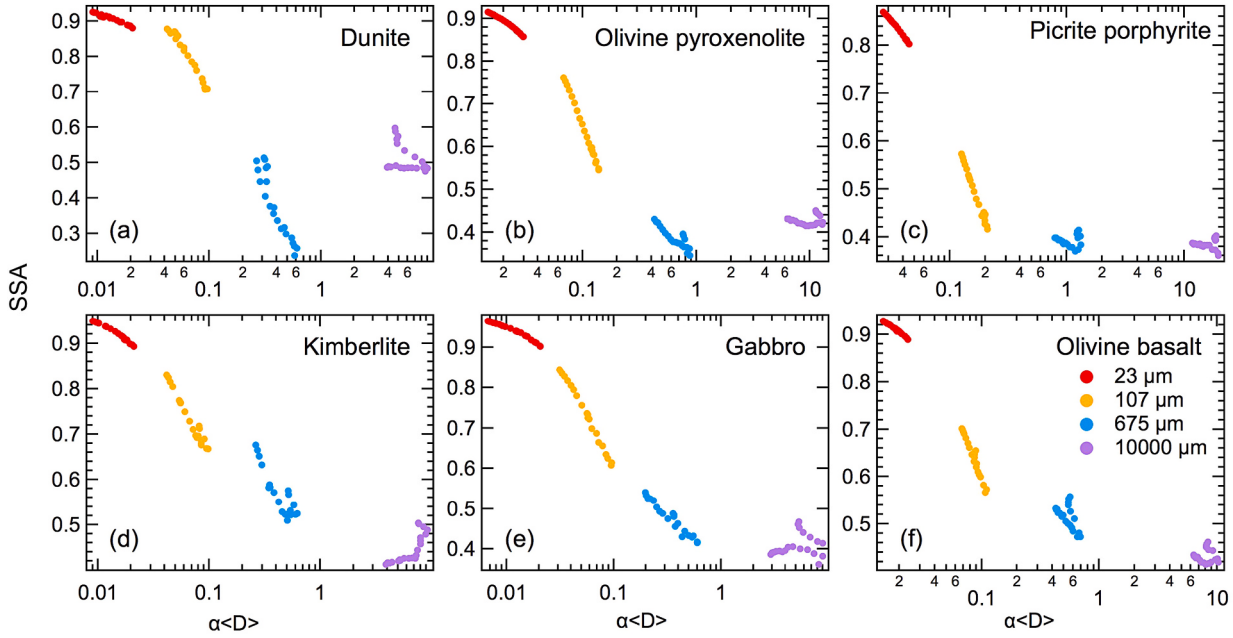


Fig. 14. Same as Fig. 13, but for samples whose slabs have less-pronounced 1 μm absorption feature.

6. Applications to Chang'E-4 data analysis

As mentioned in Section 1, when comparing the VNIR spectrum of a lunar rock measured by Chang'E-4 with the laboratory spectra of lunar-related samples, we found a powdered lunar meteorite (Yamato-86032), among others, had the best match spectrum. In order to infer how well this sample's spectra in large size may match the Chang'E-4 rock spectra, we applied the method described in Section 4.3 to the spectrum of Yamato-86032. Since the Yamato 86032 spectrum is only available for one size distribution (0–45 μm), retrieving k and s simultaneously using the method outlined in Fig. 10 is not possible. Therefore, we fixed s

to 3 typical values according to the s values obtained by the 13 igneous rock samples (Figure S12), 0.01, 0.05, and 0.1 μm^{-1} , and solved the corresponding k values using equations (5)–(15), and then input the s and k values to the model to obtain the reconstructed model spectra for different sizes. Fig. 17 shows the comparisons of the Chang'E-4 rock spectrum, the lunar meteorite powder spectrum, and the model reconstructed meteorite spectra for particle sizes of 23 μm , 675 μm and 10000 μm , both in REFF and continuum-removed REFF spectra. While most model spectra do not change much when the particle size exceeds 675 μm , there are still some differences in the model spectra of Gabbro and Trachyte. Therefore, we used two sizes of 675 μm and 10000 μm to

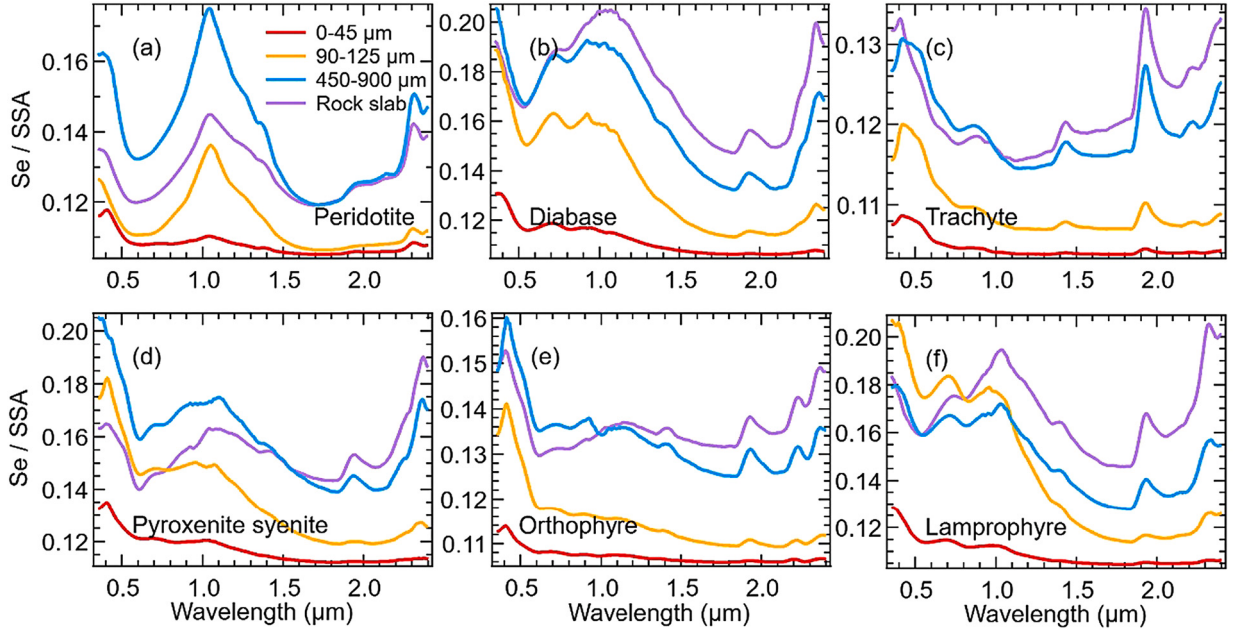


Fig. 15. Ratios of S_e to SSA for samples whose slabs have a pronounced $1 \mu\text{m}$ absorption feature.

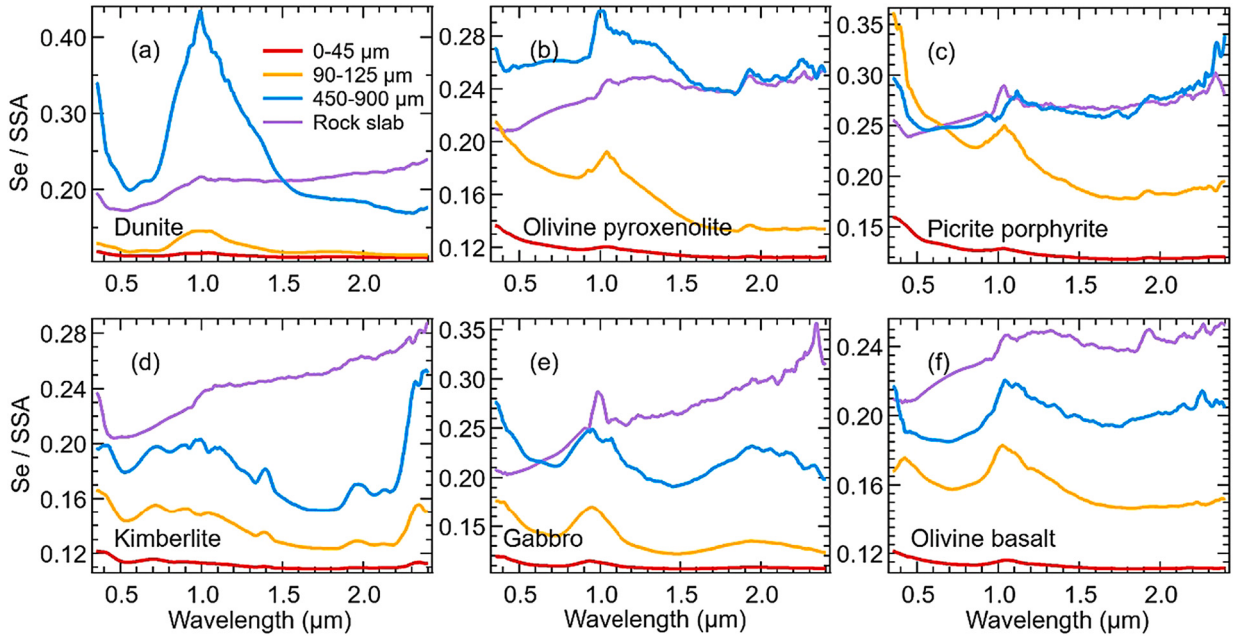


Fig. 16. Ratios of S_e to SSA for samples whose slabs have less pronounced $1 \mu\text{m}$ absorption feature.

model the slab spectra of the meteorite. These results show that the model spectra of $D = 23 \mu\text{m}$ produced using various s values can all match the meteorite powder spectrum very well, and the model spectrum of $D = 675 \mu\text{m}$ and $D = 10000 \mu\text{m}$ using $s = 0.05 \mu\text{m}^{-1}$ is closer to the Chang'E-4 rock spectrum than those using other s values. In addition to the mismatch of the $1 \mu\text{m}$ absorption peak shape, the *in-situ* lunar spectrum is redder than the model reconstructed meteorite spectrum in large size. This is not a surprise, because even if the two samples have similar mineralogical compositions, the lunar rock should have experienced more space weathering alterations than the meteorite sample, causing its redder spectrum. For the continuum-removed $REFF$, the model reconstructed spectra for $D = 675 \mu\text{m}$ using $s = 0.05 \mu\text{m}^{-1}$, $D = 10000 \mu\text{m}$ using $s = 0.01 \mu\text{m}^{-1}$ and $s = 0.05 \mu\text{m}^{-1}$ are much closer to the Chang'E-4 rock spectrum, indicating the good match of the two samples.

7. Conclusions

We have measured the visible and near-infrared reflectance spectra of 13 types of igneous rocks in slabs and in powders with three size fractions, $0-45 \mu\text{m}$, $90-125 \mu\text{m}$, and $450-900 \mu\text{m}$. We found that these samples can be divided into two groups according to the characteristic spectral feature of the slabs vs. those of the powdered samples. By fitting measurements to the equivalent-slab model and the Hapke model, we obtained the optical constants of the samples and calculated the model spectra of the samples with different particle sizes. The major conclusions are as follows:

- (1) In general, the spectral slope of the sample decreases with the increase of particle size, and as a result, most powder samples

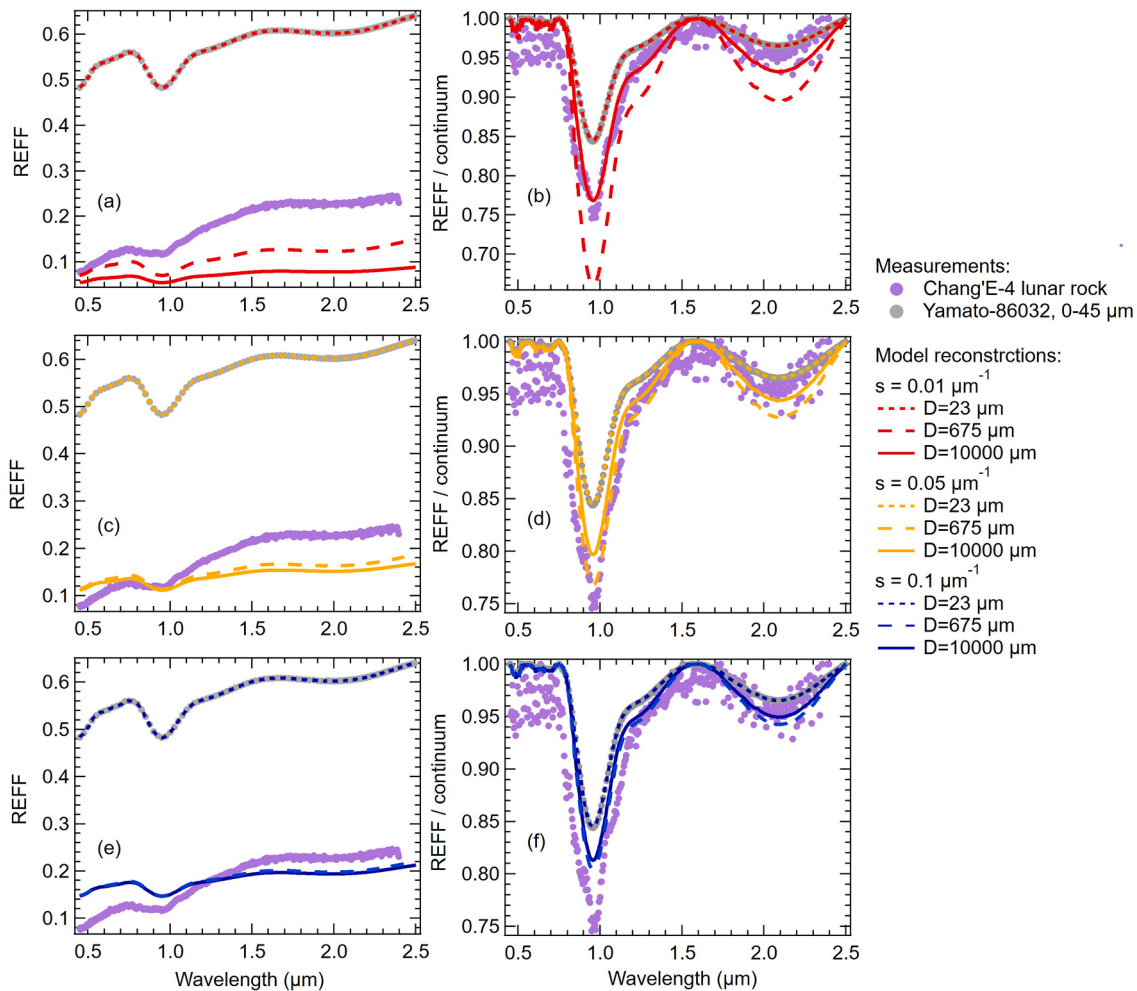


Fig. 17. Comparisons of the *in-situ* Chang'E-4 lunar rock spectrum, its best matched laboratory spectrum of powdered lunar meteorite Yamato-86032, and model reconstructed spectra for $D = 23 \mu\text{m}$ and $D = 10000 \mu\text{m}$, using 3 different internal scattering coefficient (s) values. The Yamato-86032 spectrum was measured on a fine powder with grain sizes of $0-45 \mu\text{m}$. (a), (c), (e) are the REFF spectra and (b), (d), (f) are the continuum-removed spectra. The s values used in the model reconstructed spectra are $0.01 \mu\text{m}^{-1}$ in (a) and (b), $0.05 \mu\text{m}^{-1}$ in (c) and (d), and $0.1 \mu\text{m}^{-1}$ in (e) and (f).

have a positive slope while most slab samples have a negative or neutral slope. The band position of the $1 \mu\text{m}$ absorption peak did not change with the change of the sample particle size.

- (2) Other than a few exceptions, if a slab sample's reflectance factor value $REFF(0.5\mu\text{m})$ is greater than 0.1, both its slab and powders have pronounced $1 \mu\text{m}$ absorption features; otherwise, its slab sample lack the pronounced $1 \mu\text{m}$ absorption feature compared to its powder's spectra.
- (3) Modeling results indicate that, for slab samples with a low albedo, light scattering is in the regime of weak surface scattering, where photons are inhibited from penetrating deeper into the grain interior, thereby suppressing the appearance of the $1 \mu\text{m}$ absorption feature. For brighter slab samples, particle scattering is dominated by volume scattering, and thus the absorption characteristics of the material can be fully displayed.
- (4) When the equivalent slab and the Hapke models are applied to a powdered lunar meteorite, we computed model spectra for the rocks derived from the powdered sample spectrum. These model spectra are very close to the spectrum of a rock observed *in situ* by the Chang'E-4 visible and near-infrared spectrometer instrument on the Moon thus validating our earlier findings of the best-matched laboratory sample spectra.

One implication of these results is that when the spectrum of a

particular planet's surface is found to have a blue spectral slope and no obvious absorption features, it does not necessarily mean that the material being measured is spectrally featureless. Instead, the target may consist primarily of rocky materials that may exhibit different spectral signatures when pulverized.

In future, we will study more samples to investigate whether the empirical rule found in this work is universal. Since space weathering may produce patina structures on rocks on airless bodies, the spectral signature connections between space weathered rocks and regolith will be also relevant. We also expect quantitative models of light reflection from lumpy rocks will become available in the future.

Acknowledgments, samples, and data

We thank Megha Bhatt and an anonymous reviewer for their useful comments that improved the quality of this manuscript. This work was supported by the National Natural Science Foundation of China (11941001, 12073024) and the Civil Aerospace Pre-research Project (D020302). The reflectance data can be downloaded from [Zhuang et al. \(2021\)](#).

Declaration of Competing Interest

None.

Data availability

Data download link is in the Reference: Zhuang et al., 2021.

Appendix A. Supplementary data

Supplementary data to this article can be found online at <https://doi.org/10.1016/j.icarus.2022.115346>.

References

- Adams, J.B., 1974. Visible and near-infrared diffuse reflectance spectra of pyroxenes as applied to remote sensing of solid objects in the solar system. *J. Geophys. Res.* 79, 4829–4836. <https://doi.org/10.1029/JB079i032p04829>.
- Adams, J.B., Filice, A.L., 1967. Spectral reflectance 0.4 to 2.0 microns of silicate rock powders. *J. Geophys. Res.* 72, 5705–5715. <https://doi.org/10.1029/JZ072i022p05705>.
- Bohren, C.F., 1987. Multiple scattering of light and some of its observable consequences. *American Journal of Physics* 55, 524–533. <https://doi.org/10.1119/1.15109>.
- Bruegge, C., Chrien, N., Haner, D., 2001. A Spectralon BRF data base for MISR calibration applications. *Remote Sens. Environ.* 77, 354–366. [https://doi.org/10.1016/S0034-4257\(01\)00214-0](https://doi.org/10.1016/S0034-4257(01)00214-0).
- Burbine H, Thomas, 2017. *Asteroids: Astronomical and Geological Bodies*. Cambridge.
- Carli, C., Sgavetti, M., 2011. Spectral characteristics of rocks: Effects of composition and texture and implications for the interpretation of planet surface compositions. *Icarus* 211, 1034–1048. <https://doi.org/10.1016/j.icarus.2010.11.008>.
- Chapman, C.R., 2004. Space weathering of asteroid surfaces. *Annu. Rev. Earth Planet. Sci.* 32, 539–567. <https://doi.org/10.1146/annurev.earth.32.101802.120453>.
- Clark, R.N., Roush, T.L., 1984. Reflectance spectroscopy: Quantitative analysis techniques for remote sensing applications. *J. Geophys. Res.* 89, 6329–6340. <https://doi.org/10.1029/JB089iB07p06329>.
- Di, K., Liu, Z., Liu, B., Wan, W., Peng, M., Wang, Y., Gou, S., Yue, Z., Xin, X., Jia, M., Niu, S., 2019. Chang'e-4 lander localization based on multi-source data. *Journal of Remote Sensing* 23, 181–184. <https://doi.org/10.11834/jrs.20199015>.
- Dunn, T.L., McCoy, T.J., Sunshine, J.M., McSween Jr., H.Y., 2010. A coordinated spectral, mineralogical, and compositional study of ordinary chondrites. *Icarus* 208, 789–797. <https://doi.org/10.1016/j.icarus.2010.02.016>.
- Hapke, B., 2001. Space weathering from Mercury to the asteroid belt. *J. Geophys. Res.* 106, 10039–10073. <https://doi.org/10.1029/2000JE001338>.
- Hapke, B., 2002. Bidirectional Reflectance Spectroscopy 5: The coherent backscatter opposition effect and anisotropic scattering. *Icarus* 157, 523–534. <https://doi.org/10.1006/icar.2002.6853>.
- Hapke, B., 2012. *Theory of reflectance and emittance spectroscopy*, 2nd ed. Cambridge University Press, Cambridge, UK, New York.
- Harloff, J., Arnold, G., 2001. Near-infrared reflectance spectroscopy of bulk analog materials for planetary crust. *Planetary and Space Science* 49 (2), 191–211. [https://doi.org/10.1016/S0032-0633\(00\)00132-X](https://doi.org/10.1016/S0032-0633(00)00132-X).
- Helfenstein, P., Ververka, J., Thomas, P.C., Simonelli, D.P., Klaasen, K., Johnson, T.V., Fanale, F., Granahan, J., McEwen, A.S., Belton, M., Chapman, C., 1996. Galileo Photometry of Asteroid 243 Ida. *Icarus* 120, 48–65. <https://doi.org/10.1006/icar.1996.0036>.
- Hiroi, T., Pieters, C.M., 1994. Estimation of grain sizes and mixing ratios of fine powder mixtures of common geologic minerals. *J. Geophys. Res.* 99, 10867. <https://doi.org/10.1029/94JE00841>.
- Jiang, T., Zhang, H., Yang, Y., Hu, X., Ma, P., Sun, Y., Britt, D., Wang, W., Lu, X., Huang, J., Hsu, W., Mei, B., Wei, R., 2019. Bi-directional reflectance and polarization measurements of pulse-laser irradiated airless body analog materials. *Icarus* 331, 127–147. <https://doi.org/10.1016/j.icarus.2019.05.022>.
- Jiang, T., Zhang, H., Yang, Y., Ma, P., Sun, Y., Zhuang, Y., 2022. A non-motorized spectro-goniometric system to measure the bi-directional reflectance spectra of particulate surfaces in the visible and near-infrared. *Rev. Sci. Instr.* 93, 024504. <https://doi.org/10.1063/5.0071621>.
- Jolliff, B.L., Wieczorek, M.A., Shearer, C.K., Neal, C.R., 2006. *New views of the Moon*. Mineralogical Society of America, Chantilly, VA.
- Keller, L.P., McKay, D.S., 1997. The nature and origin of rims on lunar soil grains. *Geochim. Cosmochim. Acta* 61, 2331–2341. [https://doi.org/10.1016/S0016-7037\(97\)00085-9](https://doi.org/10.1016/S0016-7037(97)00085-9).
- Lester, T.P., McCall, M.L., Tatum, J.B., 1979. Theory of planetary photometry. *J Royal Astron. Soc. Can.* 73, 233–257.
- Longhi, I., Sgavetti, M., Chiari, R., Mazzoli, C., 2001. Spectral analysis and classification of metamorphic rocks from laboratory reflectance spectra in the 0.4–2.5 μ m interval: A tool for hyperspectral data interpretation. *Int. J. Remote Sens.* 22, 3763–3782. <https://doi.org/10.1080/01431160010006980>.
- Lucey, P.G., 1998. Model near-infrared optical constants of olivine and pyroxene as a function of iron content. *J. Geophys. Res.* 103, 1703–1713. <https://doi.org/10.1029/97JE03145>.
- Ma, P., Sun, Y., Zhu, M.-H., Yang, Y., Hu, X., Jiang, T., Zhang, H., Lucey, P.G., Xu, R., Li, C., He, Z., Xue, B., Yang, J., Huang, C., Lin, H., 2020. A plagioclase-rich rock measured by Yutu-2 Rover in Von Kármán crater on the far side of the Moon. *Icarus* 350, 113901. <https://doi.org/10.1016/j.icarus.2020.113901>.
- McKay, D.S., Heiken, G., Basu, A., Blanford, G., Simon, S., Reedy, R., Papike, J., 1991. *The Lunar Regolith*. Lunar Sourcebook. Cambridge University Press.
- Mustard, J.F., Hays, J.E., 1997. Effects of Hyperfine Particles on Reflectance Spectra from 0.3 to 25 μ m. *Icarus* 125, 145–163. <https://doi.org/10.1006/icar.1996.5583>.
- Noble, S.K., Pieters, C.M., Taylor, L.A., Morris, R.V., Allen, C.C., McKay, D.S., Keller, L.P., 2001. The optical properties of the finest fraction of lunar soil: Implications for space weathering. *Meteorit. Planet. Sci.* 36, 31–42. <https://doi.org/10.1111/j.1945-5100.2001.tb01808.x>.
- Papike, J.J., Simon, S.B., Lau, J.C., 1982. The lunar regolith: Chemistry, mineralogy, and petrology. *Rev. Geophys.* 20, 761. <https://doi.org/10.1029/RG020i004p00761>.
- Paton, M., Muinonen, K., Pesonen, L.J., Kuosmanen, V., Kohout, T., Laitinen, J., Lehtinen, M., 2011. A PCA study to determine how features in meteorite reflectance spectra vary with the samples' physical properties. *J. Quant. Spectrosc. & Radiat. Transf.* 112, 1803–1814. <https://doi.org/10.1016/j.jqsrt.2011.01.033>.
- Pieters, C.M., 1983. Strength of mineral absorption features in the transmitted component of near-infrared reflected light: First results from RELAB. *J. Geophys. Res.* 88, 9534–9544. <https://doi.org/10.1029/JB088iB11p09534>.
- Pieters, C.M., Nobel, S.K., 2016. Space weathering on airless bodies. *J. Geophys. Res.* 121, 1865–1884. <https://doi.org/10.1002/2016JE005128>.
- Pieters, C.M., Fischer, E.M., Rode, O., Basu, A., 1993. Optical effects of space weathering: The role of the finest fraction. *J. Geophys. Res.* 98 (E11), 20817. <https://doi.org/10.1029/93JE02467>.
- Riner, M.A., Lucey, P.G., Desch, S.J., McCubbin, F.M., 2009. Nature of opaque components on Mercury: Insights into a Mercurian magma ocean. *Geophys. Res. Lett.* 36, L02201. <https://doi.org/10.1029/2008GL036128>.
- Sjöpblad, S., Jorda, L., Lamy, P.L., Keller, H.U., Li, J.-Y., 2012. Disk-resolved photometry of Asteroid (2867) Steins. *Icarus* 221, 1101–1118. <https://doi.org/10.1016/j.icarus.2012.06.021>.
- Sun, L., Lucey, P.G., 2021. Unmixing Mineral Abundance and Mg# With Radiative Transfer Theory: Modeling and Applications. *J. Geophys. Res. Planets* 126. <https://doi.org/10.1029/2020JE006691> e2020JE006691.
- Wentworth, S.J., Keller, L.P., McKay, D.S., Morris, R.V., 1999. Space weathering on the Moon: Patina on Apollo 17 samples 75075 and 76015. *Meteorit. Planet. Sci.* 34, 592–602. <https://doi.org/10.1111/j.1945-5100.1999.tb01366.x>.
- Yang, Y., Li, S., Milliken, R.E., Zhang, H., Robertson, K., Hiroi, T., 2019. Phase Functions of Typical Lunar Surface Minerals Derived for the Hapke Model and Implications for Visible to Near-Infrared (VNIR) Spectral Unmixing. *J. Geophys. Res. Planets* 124, 31–60. <https://doi.org/10.1029/2018JE005713>.
- Zhang, H., Voss, K.J., 2005. Comparisons of bidirectional reflectance distribution function measurements on prepared particulate surfaces and radiative-transfer models. *Appl. Opt.* 44, 597–610. <https://doi.org/10.1364/AO.44.000597>.
- Zhang, H., Voss, K.J., Reid, R.P., 2003. Determining the influential depth for surface reflectance of sediment by BRDF measurements. *Opt. Express* 11, 2654–2665. <https://doi.org/10.1364/OE.11.002654>.
- Zhang, H., Yang, Y., Jin, W., Liu, C., Hsu, W., 2014. Effects of Spectralon absorption on reflectance spectra of typical planetary surface analog materials. *Opt. Express* 22, 21280–21291. <https://doi.org/10.1364/OE.22.021280>.
- Zhuang, Y., Zhang, H., Ma, P., Jiang, T., Yang, Y., Milliken, R., Hsu, W., 2021. Visible and Near-Infrared Reflectance Spectra of Igneous Rocks and Their Powders [Data set]. Zenodo. <https://doi.org/10.5281/zenodo.5548913>.